

Active phase separation by turning toward regions of higher density

Jie Zhang,^{1,*} Ricard Alert,^{2,3,*} Jing Yan,⁴ Ned S. Wingreen,^{2,5} and Steve Granick^{6,7}

¹*Department of Physics, University of California at Santa Barbara, Santa Barbara, CA 93106, USA*

²*Lewis-Sigler Institute for Integrative Genomics, Princeton University, Princeton, NJ 08544, USA*

³*Princeton Center for Theoretical Science, Princeton University, Princeton, NJ 08544, USA*

⁴*Department of Molecular, Cellular and Developmental Biology, Yale University, New Haven, CT 06511, USA*

⁵*Department of Molecular Biology, Princeton University, Princeton, NJ 08544, USA*

⁶*Center for Soft and Living Matter, Institute for Basic Science (IBS), Ulsan 44919, South Korea*

⁷*Departments of Chemistry and Physics, Ulsan National Institute of Science and Technology (UNIST), Ulsan 44919, South Korea*

(Dated: November 23, 2021)

Studies of active matter, from molecular assemblies to animal groups, have revealed two broad classes of behavior: a tendency to align yields orientational order and collective motion, whereas particle repulsion leads to self-trapping and motility-induced phase separation. Here, we report a third class of behavior: orientational interactions that produce active phase separation. Combining theory and experiments on self-propelled Janus colloids, we show that stronger repulsion on the rear than on the front of these particles produces non-reciprocal torques that reorient particle motion toward high-density regions. Particles thus self-propel toward crowded areas, which leads to phase separation. Clusters remain fluid and exhibit fast particle turnover, in contrast to the jammed clusters that typically arise from self-trapping, and interfaces are sufficiently wide that they span entire clusters. Overall, our work identifies a torque-based mechanism for phase separation in active fluids, and our theory predicts that these orientational interactions yield coexisting phases that lack internal orientational order.

We are interested here in motile (“self-propelled”) agents. As motility naturally implies direction, alignment interactions lead to collective motion, with flocking as an iconic example. When the motility direction is not coordinated, self-propelled particles are well understood to undergo motility-induced phase separation (MIPS) under certain conditions^{1–6}. As originally conceived⁷, the mechanism of MIPS is self-trapping: Lower particle speed in high-density regions, due to quorum sensing^{7,8} or even just due to repulsive particle collisions^{9–11}, promotes continual accumulation of particles. This positive feedback leads to phase separation into a dilute gas and denser clusters. In the past decade, this scenario has been widely studied using theory and simulations^{1–6}. Proposals to realize this scenario using synthetic active colloids^{4,12–14} indeed led to the observation of motility-dependent clustering^{15–18}. Eliminating the possible role of attractive interactions, recent experiments with purely repulsive colloids have confirmed full phase separation¹⁹, or separation interrupted by the effects of aligning interactions²⁰.

Here we show that torques on motile particles can induce phase separation. This finding is surprising because torques can easily prevent MIPS. For example, rod-shaped particles experience torques that favor alignment, thereby avoiding self-trapping and suppressing MIPS^{21–25}. Other kinds of orientational interactions, including dipolar torques^{20,26,27} and velocity-alignment rules^{28–31}, can either hinder or promote standard repulsion-based MIPS. Unlike conventional MIPS, torque-based aggregation requires no density-induced slowdown, so the particles that condense into clusters retain substantial speed. As a result, clusters remain fluid, as opposed to the close-packed and jammed clusters typically obtained in repulsion-based MIPS^{9–11,19,20}. Consequently, this alternative

mechanism of phase separation has the potential to enlarge resulting group functions, such as fast turnover of active agents and efficient exchange of information.

Active phase separation in metal-dielectric Janus colloids

Here, we combine theory and experiments on self-propelled Janus particles driven by dielectrophoresis. The particles are 3 μm -diameter silica spheres, coated with titanium (Methods) on one hemisphere. These particles are suspended in a 0.05 mM NaCl aqueous solution and placed between conductive coverslips coated with indium tin oxide, separated by a 120 μm spacer (Fig. 1a, Methods). Particles sediment to form a dilute monolayer with area fraction in the range $\phi_0 \approx 0.05 - 0.15$. To drive the particles, we apply a perpendicular AC voltage of amplitude $V_0 = 8 - 10$ V and frequency $\nu = 30$ kHz. The resulting electric field tends to align the particle equator perpendicular to the coverslips. The resulting unequal electric polarization on the metal and dielectric hemispheres (Fig. 1b) induces electrokinetic flows that produce particle self-propulsion^{32–34} (along a direction \hat{n} pointing from the metallic to the dielectric hemisphere), as well as electrostatic interparticle forces and torques (Fig. 1b).

Clusters, observed within seconds after switching on the electric field, coarsen in a process suggestive of Ostwald ripening, with large clusters growing and small clusters shrinking and disappearing (Movie 1, Fig. S1). Domain-growth kinetics are compatible with the Lifshitz-Slyozov relation $L(t) \sim t^{1/3}$ of classic phase separation (Fig. 1c), consistent with the mapping to an effective free energy we present below.

As some particles stuck on the coverslip were not possible to avoid experimentally, it was natural to inquire whether clusters necessarily nucleated around them. This possibility was discounted as at early times the majority of clusters encompassed no stuck particles (Fig. S2). On the other hand, during coarsening a large fraction of clusters contain a few particles

* These authors contributed equally to this work.

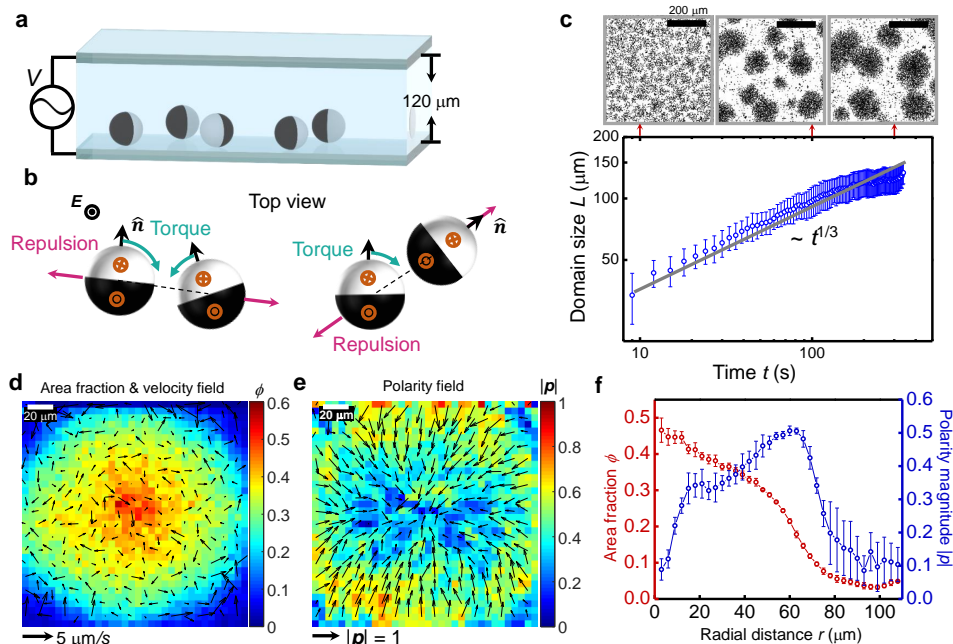


Figure 1 | Active phase separation in metal-dielectric Janus colloids. **a**, Schematic of the experimental setup in which $3\ \mu\text{m}$ -diameter particles are allowed to sediment in water to the bottom of a sample cell across which AC electric fields are applied vertically. **b**, Top view of two Janus particle pairs in an electric field that induces dipoles of opposite orientation and different magnitude (orange) on the head and tail hemispheres. This leads to particle self-propulsion along the direction \hat{n} (black), and to interparticle forces (purple) and torques (green). Torques rotate particles in the direction of the interparticle distance, which is indicated by the dashed line. These torques are generally non-reciprocal. **c**, Clusters coarsen (Movie 1, 30 kHz, 83 V/mm) with domain-growth kinetics compatible with the Lifshitz-Slyozov relation $L(t) \sim t^{1/3}$. Error bars are S.D. over four independent experiments. **d,e**, Time-averaged local area fraction (**d**, color), along with velocity field (**d**, arrows) and polarity field (**e**, arrows with magnitude in color) in a cluster (30 kHz, 66 V/mm). Averaging is over $6\ \mu\text{m}$ square bins over 50 s (2500 frames), during which the number of particles in the cluster remains approximately constant (Fig. S4). **f**, Angle-averaged radial profiles of area fraction (red) and polarity magnitude (blue) corresponding to panels **d** and **e**. Error bars are S.D.

that are stuck on the coverslip, which might help form and stabilize the clusters (Fig. S2).

Clusters have wide interfaces

Despite the familiar coarsening kinetics, the structure and dynamics of individual clusters differ markedly from those observed in passive phase separation and repulsion-based MIPS. Rather than displaying the standard uniform bulk and sharp interface, our clusters exhibit a pronounced density gradient (Figs. 1d and S3, and Movie 2) and inward-pointing polarity (Fig. 1e), defined as $\mathbf{p} = \langle \hat{n} \rangle$. Particle density increases from the edge to the center without a density plateau (Fig. 1f, red) for clusters up to $\sim 300\ \mu\text{m}$ in diameter, suggesting very wide interfaces, at least several tens of micrometers. The central density (area fraction $\phi \sim 0.6$) never approaches close packing. Reciprocally, polarity $|\mathbf{p}|$ is highest at the cluster edge and decreases toward the center (Fig. 1f, blue). This decrease suggests that clusters might eventually grow large enough to develop an isotropic ($\mathbf{p} = 0$) bulk phase. The inward-pointing polarity at clusters' edges prevents them from coalescing immediately upon contact. Rather, upon collisions between clusters, visible boundaries persist for up to minutes (Movie 1, see snapshots in Fig. 1c).

Non-jammed clusters with fast particle turnover

The dynamics of individual particles within clusters differs markedly from that in jamming-based MIPS: Clusters are fluid, not jammed. Particles move easily through clusters (Movie 3), which exhibit fast turnover, with particles leaving and joining a cluster on a time scale of tens of seconds (Fig. 2a). The number of native particles that remain in a cluster decays exponentially with a characteristic time depending on the cluster size and particle speed (Figs. 2b and S5, and Movie 4). By tracking particle position and orientation at different local area fractions ϕ , we obtain their mean square translational and angular displacements (Fig. S6). From these measurements, we find that particles within clusters ($\phi > 0.1$) are slower than those outside them ($\phi < 0.1$), but do not slow down further at the higher densities deeper inside clusters (Fig. 2c, red). On the other hand, the effective rotational diffusivity D_r^{eff} increases monotonically with local area fraction (Fig. 2c, blue), indicating faster particle reorientations due to stronger interparticle torques in denser regions.

Flickering chains facilitate particle motion

Since head and tail particle hemispheres attract each other (Fig. 1b), particles in clusters often form chains, 3-7 particles long, which last hundreds of milliseconds (Movie 5, red lines

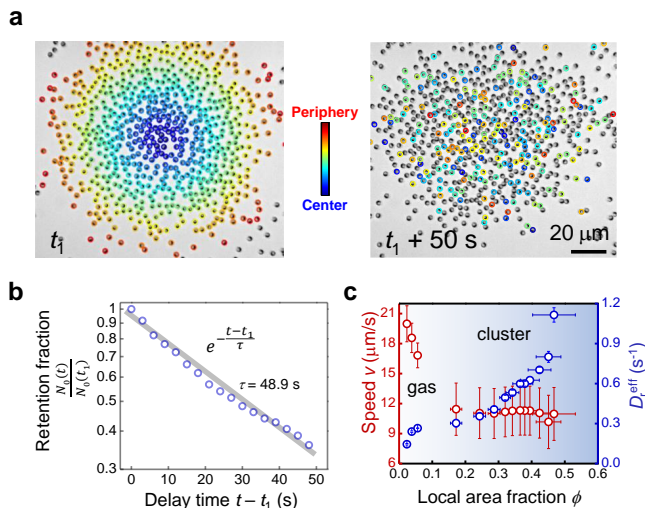


Figure 2 | Particle turnover dynamics of non-jammed clusters whose population remains nearly constant. **a**, Example of particle turnover between the gas and cluster states for a cluster whose total population is nearly constant over the experimental time window (Movie 3). The first snapshot shows the cluster at an initial time $t = t_1$, chosen arbitrarily, with particles colored according to their distance from the cluster centroid. In the second snapshot, 50 s later, particles have moved through the cluster and turned over. **b**, Particle retention dynamics. The fraction of initial particles that remain within the cluster decays exponentially with elapsed time. **c**, Average particle speed (red) and effective rotational diffusivity (blue) within the gas and cluster states, as functions of the local area fraction. The three points at low area fractions ($\phi < 0.1$) correspond to the gas state. Increasingly higher area fractions correspond to regions deeper into clusters. The speed and effective rotational diffusivity are obtained from the first 0.5 s of the translational and angular mean squared displacements, respectively (Fig. S6). Averaging is over 50 s (2500 frames) in the cluster shown in panel **a**. Error bars are S.D.

in Fig. 3a). These chains constantly deform, break, and reform, with particles hopping on and off different chains. To characterize positional and orientational order, we measure the pair distribution function $g(\mathbf{r}) = \phi(\mathbf{r})/\phi_0$ and the orientation correlation function $C(\mathbf{r}) = \langle \hat{\mathbf{n}}(\mathbf{r}') \cdot \hat{\mathbf{n}}(\mathbf{r}' + \mathbf{r}) \rangle$. As expected for self-propelled particles, $g(\mathbf{r})$ is anisotropic; it is more likely to find another particle ahead than behind a reference particle (Fig. 3b). We also find that it is more likely to find another particle behind than on the side of the reference particle, producing a depletion wing pattern (Fig. 3c). While recent work showed that these depletion wings can arise even in the absence of alignment interactions³⁵, in our system they result from torques generated by head-tail attraction. Finally, orientational correlations are stronger along the direction of self-propulsion than perpendicular to it (Fig. 3c), showing that particles tend to align along the chains, but not with lateral neighbors.

Particle orientation and velocity are misaligned in clusters

Despite these transient chains, particle motion is disordered

at long times, as shown by the time-averaged velocity field (Fig. 1d, arrows). Interestingly, this lack of velocity order coexists with radial polar order (Fig. 1e). This distinction is apparent in the probability distributions of the angles formed by the particle orientation and velocity with respect to the clusters' radial direction (Fig. 3d): Whereas the orientation angle distribution peaks at 0 (Fig. 3e, blue), consistent with radial order, the velocity angle distribution peaks at $\pm\pi/2$ (Fig. 3e, red), indicating flows orthogonal to the radial direction. I.e., even though particles orient mainly towards the center of the cluster, they have a higher chance to move tangentially to it. As expected, the difference between orientation and velocity angles is absent prior to cluster formation (Fig. S7), but emerges from the stronger interparticle interactions within clusters (Fig. 3f).

Model for Janus particles with electrostatic interactions

As our experiments show MIPS without substantial self-trapping, non-standard mechanisms might be responsible for phase separation in our system. We therefore developed a microscopic model based on the dipolar interactions between the hemispheres of our particles (SI Section A and Fig. S8). Our model shows that two particles interact via a repulsive force

$$\mathbf{F}_{ij} \approx \frac{3}{4\pi\epsilon} \frac{(d_h + d_t)^2}{r_{ij}^4} e^{-r_{ij}/\lambda} \hat{\mathbf{r}}_{ij}, \quad (1)$$

where ϵ is the dielectric permittivity of the solvent, $\mathbf{r}_{ij} = \mathbf{r}_j - \mathbf{r}_i$ is the distance vector, and $d_h < 0$ and $d_t > 0$ are the effective dipole strengths of the head and tail hemispheres, respectively (Fig. 1b). The exponential factor accounts for screening by the electrodes, separated by a distance $\lambda = 120 \mu\text{m}$. Moreover, because tail dipoles are stronger than head dipoles ($d_t^2 > d_h^2$), particles interact via a torque

$$\mathbf{\Gamma}_{ij} \approx \frac{3\ell}{4\pi\epsilon} \frac{d_h^2 - d_t^2}{r_{ij}^4} e^{-r_{ij}/\lambda} \hat{\mathbf{n}}_j \times \hat{\mathbf{r}}_{ij}, \quad (2)$$

where $\ell = 3R/8$ is the distance by which the dipoles are off-centered, with $R = 1.5 \mu\text{m}$ the particle radius. This torque tends to reorient the particles in the direction of the interparticle distance vector \mathbf{r}_{ij} (Fig. 1b). Hence, this torque is responsible for chain formation (Fig. 3); particles aligned in a chain experience no torque because they point along \mathbf{r}_{ij} (Fig. 1b, right). Even though the underlying forces between dipoles are reciprocal, the torques $\mathbf{\Gamma}_{ij}$ between particles are in general non-reciprocal: $\mathbf{\Gamma}_{ij} \neq -\mathbf{\Gamma}_{ji}$. Whereas one particle may be already aligned with the interparticle distance \mathbf{r}_{ij} , the other one may not (Fig. 1b, right). As two particles reorient in a non-reciprocal way, they also rotate around their common center of mass (SI Section A). Experimentally, torque non-reciprocity manifests in the dynamics and statistics of two-particle interaction events (Fig. S9).

We write Langevin equations for the translational and rota-

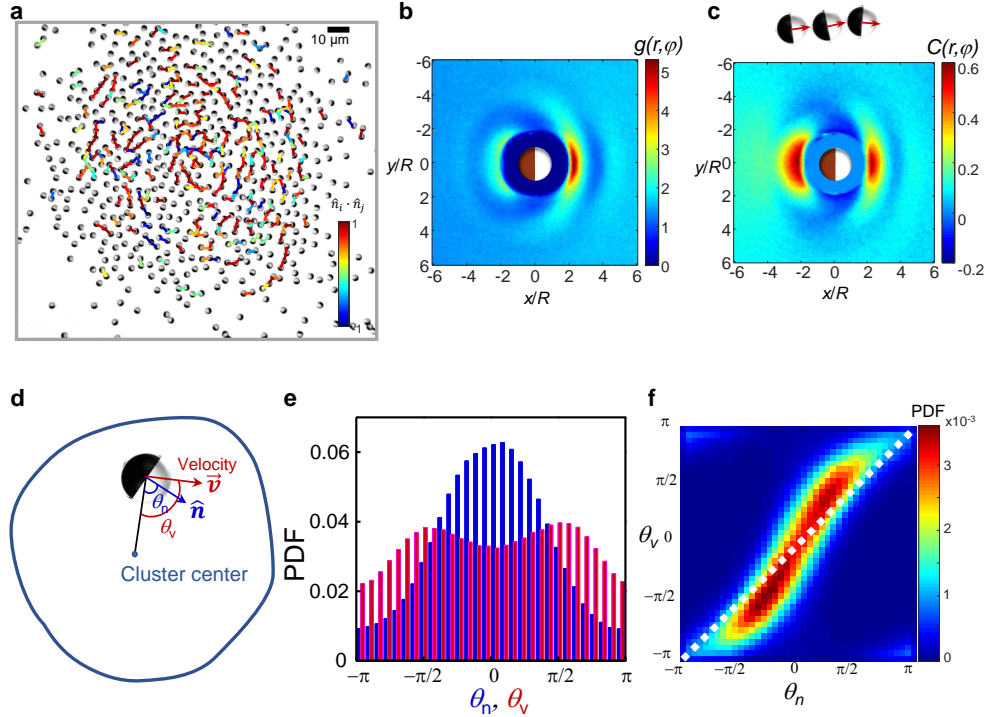


Figure 3 | Particle orientation, velocity, and correlations in non-jammed clusters. **a**, Snapshot of a cluster, overlaid with lines connecting pairs of particles whose centers are separated by less than 3 particle radii. The color map shows the degree of pair alignment, with red indicating chaining. **b,c**, Pair distribution $g(\mathbf{r})$ and orientation correlation $C(\mathbf{r})$ averaged over the cluster for 50 s (2500 frames), showing the tendency of particles to line up and align in chains, respectively. Coordinates are scaled by the particle radius. **d**, Definitions of the angle formed by particle orientation (θ_n) and velocity (θ_v) with respect to the radial direction. Schematically, the blue contour indicates the cluster periphery. **e,f**, Individual (**e**) and joint (**f**) probability distribution functions (PDFs) of the orientation and velocity angles defined in **d**. In **f**, deviation from the diagonal shows misalignment between particle orientation and velocity.

tional motion of particle i as

$$\frac{d\mathbf{r}_i}{dt} = v_0 \hat{\mathbf{n}}_i + \frac{\mathbf{F}_i}{\xi_t} + \boldsymbol{\eta}_i^t(t); \quad \mathbf{F}_i = \sum_{j \neq i} \mathbf{F}_{ji}, \quad (3a)$$

$$\frac{d\hat{\mathbf{n}}_i}{dt} = \frac{\boldsymbol{\Gamma}_i}{\xi_r} + \boldsymbol{\eta}_i^r(t); \quad \boldsymbol{\Gamma}_i = \sum_{j \neq i} \boldsymbol{\Gamma}_{ji}, \quad (3b)$$

where v_0 is the self-propulsion speed, ξ_t and ξ_r are the translational and rotational friction coefficients, respectively, and $\boldsymbol{\eta}_i^t(t)$ and $\boldsymbol{\eta}_i^r(t)$ are both Gaussian white noise (SI Section A).

Collective forces and torques

To predict the collective behavior of the system, we coarse-grain the microscopic model (SI Section B) and obtain the Smoluchowski equation for the probability $\Psi_1(\mathbf{r}, \hat{\mathbf{n}}; t)$ of finding a particle at position \mathbf{r} and orientation $\hat{\mathbf{n}}$ at time t (Eq. (S24)). This probability evolves under the action of collective interaction forces and torques that depend on the particle density field $\rho(\mathbf{r})$ ^{5,36,37}. To first order in density gradients, we obtain (SI Section B)

$$\mathbf{F}_{\text{int}}(\mathbf{r}, \hat{\mathbf{n}}) = -\Psi_1(\mathbf{r}, \hat{\mathbf{n}}) [\zeta_0 \rho(\mathbf{r}) \hat{\mathbf{n}} + \zeta_1 \nabla \rho(\mathbf{r})], \quad (4a)$$

$$\boldsymbol{\Gamma}_{\text{int}}(\mathbf{r}, \hat{\mathbf{n}}) = \Psi_1(\mathbf{r}, \hat{\mathbf{n}}) \tau_1 \hat{\mathbf{n}} \times \nabla \rho(\mathbf{r}). \quad (4b)$$

The coefficients $\zeta_0, \zeta_1, \tau_1 > 0$ (Eq. (S37)) depend on the pair distribution function $g(\mathbf{r})$ in the uniform state, which we measure in experiments (Fig. S10). Due to the higher probability of finding other particles in front of rather than behind the probe particle, the first contribution in Eq. (4a) gives a repulsion-induced force that opposes self-propulsion^{5,11} (Fig. 4a). The higher the particle density, the higher the opposing force; the resulting density-induced slowdown produces standard self-trapping MIPS familiar from extensive theoretical study^{1-6,9-11}. The second contribution in Eq. (4a) predicts a repulsion-induced force against density gradients, tending to homogenize particle concentration like a diffusive flux (Fig. 4a). Finally, the collective torque in Eq. (4b) tends to align particle orientation $\hat{\mathbf{n}}$ with the density gradient, thus reorienting particle motion *toward* higher-density regions (Fig. 4a), as observed at the clusters edges in experiments (Figs. 1d to 1f). This collective torque requires non-reciprocity of the interparticle torques (Eq. (2)). Reciprocal torques, such as $\boldsymbol{\Gamma}_{ij} \propto \hat{\mathbf{n}}_i \times \hat{\mathbf{n}}_j$, could not orient particles toward the location of other particles, and hence $\boldsymbol{\Gamma}_{\text{int}}$ would vanish^{23,24} (SI Section B). Finally, while non-reciprocal torques can lead to chiral phases³⁸, we do not find them here.

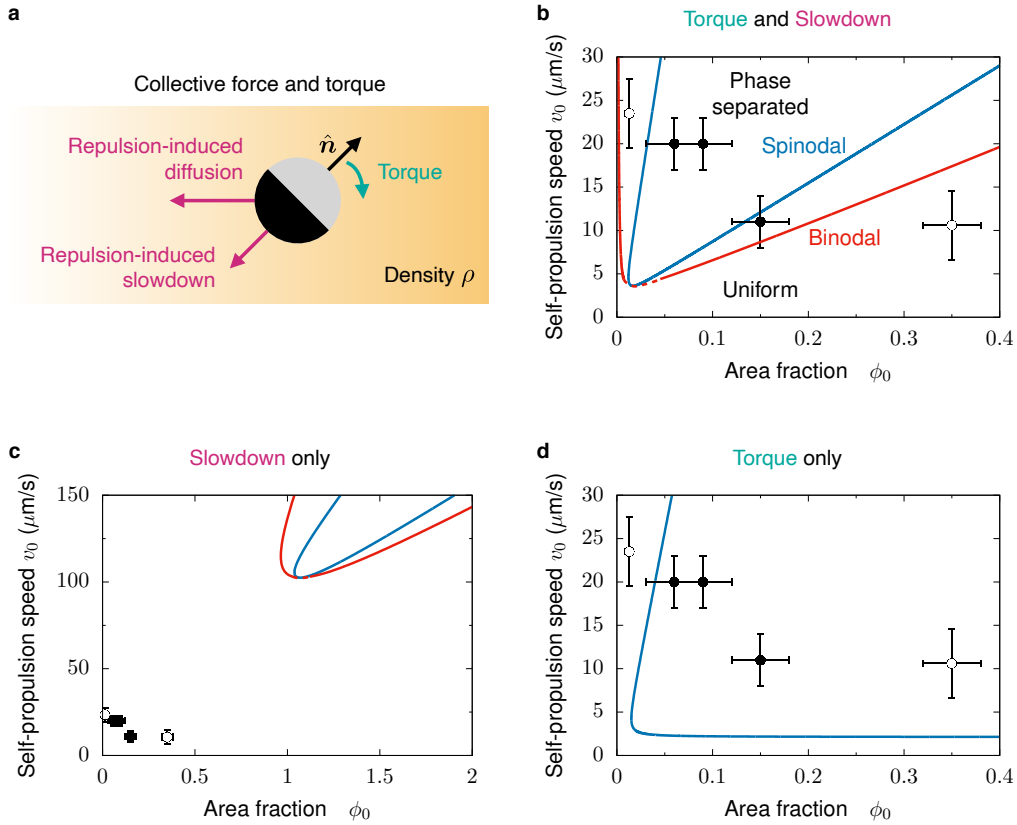


Figure 4 | State diagram of torque-based active phase separation. **a**, In the theoretical model, a probe particle experiences collective interaction force and torque (Eq. (4)) in a particle density field $\rho(\mathbf{r})$, which increases from left to right in this depiction. Repulsion leads to two collective forces (purple): one opposite to self-propulsion (slowdown), and one opposite to the density gradient (diffusion). Collective torques (green) tend to align particle motion with density gradients. **b**, State boundaries (curves) predicted using experimental estimates for parameter values (Table I in SI Section D). The numerically-unresolved region of the binodal near the critical point is indicated by a dashed curve as a guide to the eye. The filled and open data points show the experimental conditions for which phase separation was observed or not, respectively. **c**, State diagram predicted from slowdown only, i.e. $\tau_1 = 0$. Note the different scale from panel **b**. **d**, State diagram predicted from torques only, i.e. $\zeta_0 = 0$. Note the absence of binodal in this case. Error bars are S.D. obtained as in Fig. 2c.

Torque-based phase separation

As particles reorient toward crowded areas, they self-propel up their own density gradient (Fig. 4a). Hence, particles migrate toward crowded regions, which produces an instability promoting phase separation. Similar behavior was observed in active agents with finite vision cones^{39–41}. To predict the instability, we complete the coarse-graining and obtain hydrodynamic equations (SI Section B). The density field follows a continuity equation,

$$\partial_t \rho = -\nabla \cdot \mathbf{J}; \quad \mathbf{J} = v[\rho] \mathbf{p} - (D_t + D_{\text{rep}}[\rho]) \nabla \rho, \quad (5)$$

where the flux includes contributions from self-propulsion at a density-dependent speed $v[\rho(\mathbf{r})] = v_0 - \zeta_0 \rho(\mathbf{r})/\xi_t$, and diffusion that combines both bare and repulsion-induced diffusivities, D_t and $D_{\text{rep}}[\rho(\mathbf{r})] = \zeta_1 \rho(\mathbf{r})/\xi_t$, respectively. At times $t \gg D_r^{-1}$, the polarity field \mathbf{p} becomes slaved to the density field (SI Section C):

$$\mathbf{p} = \frac{1}{2D_r} (v_{\text{tor}}[\rho] \nabla \rho - \nabla(v[\rho]\rho)), \quad (6)$$

where the density-dependent speed $v_{\text{tor}}[\rho(\mathbf{r})] = \tau_1 \rho(\mathbf{r})/\xi_r$ embodies the effects of torques in polarizing the system toward increasing densities. Introducing Eq. (6) into Eq. (5), we obtain $\mathbf{J} = -\mathcal{D}[\rho] \nabla \rho$, where

$$\mathcal{D}[\rho] = D_t + D_{\text{rep}}[\rho] + \frac{v[\rho]}{2D_r} (v[\rho] + v'[\rho]\rho - v_{\text{tor}}[\rho]) \quad (7)$$

is a collective diffusivity. Thus, a uniform state with density ρ_0 experiences a spinodal instability for $\mathcal{D}(\rho_0) < 0$. In the absence of interaction torques ($v_{\text{tor}}[\rho] = 0$), \mathcal{D} can turn negative due to repulsion-induced slowdown ($v'[\rho] < 0$), which is the standard mechanism for MIPS¹. Here, Eq. (7) shows that, even in the absence of slowdown ($v'[\rho] = 0$), torques alone ($v_{\text{tor}}[\rho] > 0$) can produce a MIPS-like instability.

Furthermore, we establish that the torque-induced instability leads to phase coexistence. To this end, we express the particle flux \mathbf{J} as deriving from an effective chemical potential $\mu[\rho]$ ^{1,42–48}: $\mathbf{J} = -M[\rho] \nabla \mu[\rho]$, with $M[\rho]$ the mobility functional (SI Section C). We then use the relation $f'(\rho) = \mu(\rho)$ to obtain a local effective free energy $f(\rho)$, which has the con-

ventional double-well shape (Fig. S11). Ignoring non-local corrections^{1,43,47,48}, we use the common-tangent construction on $f(\rho)$ to predict the densities of the coexisting phases, i.e. the binodal lines of the phase diagram (SI Section C). Importantly, our theory predicts that these uniform-density phases have no orientational order (see Eq. (6)). Our theory is approximate; hence, we do not expect the predicted binodal lines to be quantitatively accurate. Yet, the existence of phase coexistence is a robust prediction which relies only on two ingredients: the torques toward dense regions and the decrease of particle speed at high densities (SI Section C). In our experiments, clusters do not achieve uniform bulk density (Fig. 1f), and therefore we are unable to observe the predicted phase coexistence. This fact suggests to us that the experimental system is in a dynamical regime whose asymptotic behavior at very large cluster size was not yet achieved.

To compare our predictions to experiments, we estimate the values of all the model parameters, including the particles' translational and rotational diffusion and friction coefficients, as well as the strength of the electric dipoles (SI Section D). These estimates allow us to predict the phase diagram in the conditions of our experiments. Our experimental observations of phase separation fall within the predicted region of the phase diagram when we include both the slowdown and torque effects (Fig. 4b). Similarly, the absence of phase separation at high area fraction also agrees with our predictions (Fig. 4b). In the uniform high-density state, we observe transient particle chains throughout the system (Movie 6, Fig. S12). With slowdown only, we cannot account for our experimental observations; the predicted phase-separation region lies at much higher self-propulsion speeds and densities than experimentally observed (Fig. 4c). Conversely, while torques alone can account for the instability of the uniform phase (spinodal in Fig. 4d), they do not yield phase coexistence (no binodal in Fig. 4d). Repulsion-induced slowdown is required to stabilize the dense phase.

In summary, we have demonstrated a new type of active phase separation based on non-reciprocal torques. Active agents reorient themselves toward crowded areas to form structured clusters, while moving easily within clusters and

also into and out of them. Perhaps more fundamentally, our theory shows that orientational interactions (torques) can produce phases of matter without internal orientational order. Our work thus establishes connections between the paradigms of aligning and non-aligning active matter, contributing to the understanding of how different types of interparticle interactions can yield qualitatively new kinds of collective nonequilibrium phenomena^{49–52}.

Acknowledgments

J.Z. and S.G. were supported by the taxpayers of South Korea through the Institute of Basic Science, project code IBS-R020-D1. R.A. thanks Julien Tailleur for insightful discussions, and acknowledges discussions with the participants of the virtual “Active 20” KITP program, supported in part by the National Science Foundation under Grant No. NSF PHY-1748958. R.A. acknowledges support from the Human Frontier Science Program (LT000475/2018-C). J.Y. holds a Career Award at the Scientific Interface from the Burroughs Wellcome Fund. N.S.W. acknowledges support from the National Science Foundation, through the Center for the Physics of Biological Function (PHY-1734030).

Author contributions

J.Z., J.Y., and S.G. conceived the experiment. J.Z. performed the experiments and analyzed data with help from J.Y. R.A. conceived and developed the theory and analyzed data. N.S.W. supervised the theory. All authors discussed and interpreted the results. J.Z., R.A., N.S.W., and S.G. wrote the manuscript.

Competing interests

The authors declare no competing interests.

Data availability

All data are available from the authors upon request.

Code availability

All codes are available from the authors upon request.

-
1. Cates, M. E. & Tailleur, J. Motility-Induced Phase Separation. *Annu. Rev. Condens. Matter Phys.* **6**, 219–244 (2015).
 2. Gonnella, G., Marenduzzo, D., Suma, A. & Tiribocchi, A. Motility-induced phase separation and coarsening in active matter. *Comptes Rendus Phys.* **16**, 316–331 (2015).
 3. Marchetti, M. C., Fily, Y., Henkes, S., Patch, A. & Yllanes, D. Minimal model of active colloids highlights the role of mechanical interactions in controlling the emergent behavior of active matter. *Curr. Opin. Colloid Interface Sci.* **21**, 34–43 (2016).
 4. Zöttl, A. & Stark, H. Emergent behavior in active colloids. *J. Phys. Condens. Matter* **28**, 253001 (2016).
 5. Speck, T. Collective forces in scalar active matter. *Soft Matter* **16**, 2652–2663 (2020).
 6. Ma, Z., Yang, M. & Ni, R. Dynamic Assembly of Active Colloids: Theory and Simulation. *Adv. Theory Simulations* **3**, 2000021 (2020).
 7. Tailleur, J. & Cates, M. E. Statistical Mechanics of Interacting Run-and-Tumble Bacteria. *Phys. Rev. Lett.* **100**, 218103 (2008).
 8. Rein, M., Heinß, N., Schmid, F. & Speck, T. Collective Behavior of Quorum-Sensing Run-and-Tumble Particles under Confinement. *Phys. Rev. Lett.* **116**, 058102 (2016).
 9. Fily, Y. & Marchetti, M. C. Athermal Phase Separation of Self-Propelled Particles with No Alignment. *Phys. Rev. Lett.* **108**, 235702 (2012).
 10. Redner, G. S., Hagan, M. F. & Baskaran, A. Structure and Dynamics of a Phase-Separating Active Colloidal Fluid. *Phys. Rev. Lett.* **110**, 055701 (2013).
 11. Bialké, J., Löwen, H. & Speck, T. Microscopic theory for the phase separation of self-propelled repulsive disks. *EPL (Europhysics Lett.)* **103**, 30008 (2013).
 12. Aranson, I. S. Active colloids. *Physics-Uspekhi* **56**, 79–92 (2013).

13. Bechinger, C. *et al.* Active Particles in Complex and Crowded Environments. *Rev. Mod. Phys.* **88**, 045006 (2016).
14. Zhang, J., Luijten, E., Grzybowski, B. A. & Granick, S. Active colloids with collective mobility status and research opportunities. *Chem. Soc. Rev.* **46**, 5551–5569 (2017).
15. Theurkauff, I., Cottin-Bizonne, C., Palacci, J., Ybert, C. & Bocquet, L. Dynamic Clustering in Active Colloidal Suspensions with Chemical Signaling. *Phys. Rev. Lett.* **108**, 268303 (2012).
16. Palacci, J., Sacanna, S., Steinberg, A. P., Pine, D. J. & Chaikin, P. M. Living crystals of light-activated colloidal surfers. *Science* **339**, 936–40 (2013).
17. Buttinoni, I. *et al.* Dynamical Clustering and Phase Separation in Suspensions of Self-Propelled Colloidal Particles. *Phys. Rev. Lett.* **110**, 238301 (2013).
18. Ginot, F., Theurkauff, I., Detscherry, F., Ybert, C. & Cottin-Bizonne, C. Aggregation-fragmentation and individual dynamics of active clusters. *Nat. Commun.* **9**, 696 (2018).
19. Geyer, D., Martin, D., Tailleur, J. & Bartolo, D. Freezing a Flock: Motility-Induced Phase Separation in Polar Active Liquids. *Phys. Rev. X* **9**, 031043 (2019).
20. van der Linden, M. N., Alexander, L. C., Aarts, D. G. A. L. & Dauchot, O. Interrupted Motility Induced Phase Separation in Aligning Active Colloids. *Phys. Rev. Lett.* **123**, 098001 (2019).
21. Shi, X.-q. & Chaté, H. Self-Propelled Rods: Linking Alignment-Dominated and Repulsion-Dominated Active Matter (2018). arXiv:1807.00294.
22. van Damme, R., Rodenburg, J., van Roij, R. & Dijkstra, M. Interparticle torques suppress motility-induced phase separation for rodlike particles. *J. Chem. Phys.* **150**, 164501 (2019).
23. Jayaram, A., Fischer, A. & Speck, T. From scalar to polar active matter: Connecting simulations with mean-field theory. *Phys. Rev. E* **101**, 022602 (2020).
24. Großmann, R., Aranson, I. S. & Peruani, F. A particle-field approach bridges phase separation and collective motion in active matter. *Nat. Commun.* **11**, 5365 (2020).
25. Bär, M., Großmann, R., Heidenreich, S. & Peruani, F. Self-Propelled Rods: Insights and Perspectives for Active Matter. *Annu. Rev. Condens. Matter Phys.* **11**, 441–466 (2020).
26. Pu, M., Jiang, H. & Hou, Z. Reentrant phase separation behavior of active particles with anisotropic Janus interaction. *Soft Matter* **13**, 4112–4121 (2017).
27. Liao, G.-J., Hall, C. K. & Klapp, S. H. L. Dynamical self-assembly of dipolar active Brownian particles in two dimensions. *Soft Matter* **16**, 2208–2223 (2020).
28. Farrell, F. D. C., Marchetti, M. C., Marenduzzo, D. & Tailleur, J. Pattern Formation in Self-Propelled Particles with Density-Dependent Motility. *Phys. Rev. Lett.* **108**, 248101 (2012).
29. Barré, J., Chétrite, R., Muratori, M. & Peruani, F. Motility-Induced Phase Separation of Active Particles in the Presence of Velocity Alignment. *J. Stat. Phys.* **158**, 589–600 (2014).
30. Sesé-Sansa, E., Pagonabarraga, I. & Levis, D. Velocity alignment promotes motility-induced phase separation. *EPL (Europhysics Lett.)* **124**, 30004 (2018).
31. Bhattacharjee, B. & Chaudhuri, D. Re-entrant phase separation in nematically aligning active polar particles. *Soft Matter* **15**, 8483–8495 (2019).
32. Gangwal, S., Cayre, O. J., Bazant, M. Z. & Velev, O. D. Induced-Charge Electrophoresis of Metallo-dielectric Particles. *Phys. Rev. Lett.* **100**, 058302 (2008).
33. Moran, J. L. & Posner, J. D. Phoretic Self-Propulsion. *Annu. Rev. Fluid Mech.* **49**, 511–540 (2017).
34. Yan, J. *et al.* Reconfiguring active particles by electrostatic imbalance. *Nat. Mater.* **15**, 1095–1099 (2016).
35. Poncet, A., Bénichou, O., Démery, V. & Nishiguchi, D. Pair correlation of dilute active Brownian particles: From low-activity dipolar correction to high-activity algebraic depletion wings. *Phys. Rev. E* **103**, 012605 (2021).
36. Kirkwood, J. G., Buff, F. P. & Green, M. S. The Statistical Mechanical Theory of Transport Processes. III. The Coefficients of Shear and Bulk Viscosity of Liquids. *J. Chem. Phys.* **17**, 988–994 (1949).
37. Irving, J. H. & Kirkwood, J. G. The Statistical Mechanical Theory of Transport Processes. IV. The Equations of Hydrodynamics. *J. Chem. Phys.* **18**, 817–829 (1950).
38. Fruchart, M., Hanai, R., Littlewood, P. B. & Vitelli, V. Non-reciprocal phase transitions. *Nature* **592**, 363–369 (2021).
39. Barberis, L. & Peruani, F. Large-Scale Patterns in a Minimal Cognitive Flocking Model: Incidental Leaders, Nematic Patterns, and Aggregates. *Phys. Rev. Lett.* **117**, 248001 (2016).
40. Durve, M., Saha, A. & Sayeed, A. Active particle condensation by non-reciprocal and time-delayed interactions. *Eur. Phys. J. E* **41**, 49 (2018).
41. Lavergne, F. A., Wendehenne, H., Bäuerle, T. & Bechinger, C. Group formation and cohesion of active particles with visual perception-dependent motility. *Science* **364**, 70–74 (2019).
42. Stenhammar, J., Tiribocchi, A., Allen, R. J., Marenduzzo, D. & Cates, M. E. Continuum Theory of Phase Separation Kinetics for Active Brownian Particles. *Phys. Rev. Lett.* **111**, 145702 (2013).
43. Wittkowski, R. *et al.* Scalar $\phi(4)$ field theory for active-particle phase separation. *Nat. Commun.* **5**, 4351 (2014).
44. Speck, T., Bialké, J., Menzel, A. M. & Löwen, H. Effective Cahn-Hilliard Equation for the Phase Separation of Active Brownian Particles. *Phys. Rev. Lett.* **112**, 218304 (2014).
45. Speck, T., Menzel, A. M., Bialké, J. & Löwen, H. Dynamical mean-field theory and weakly non-linear analysis for the phase separation of active Brownian particles. *J. Chem. Phys.* **142**, 224109 (2015).
46. Paliwal, S., Rodenburg, J., van Roij, R. & Dijkstra, M. Chemical potential in active systems: predicting phase equilibrium from bulk equations of state? *New J. Phys.* **20**, 015003 (2018).
47. Solon, A. P., Stenhammar, J., Cates, M. E., Kafri, Y. & Tailleur, J. Generalized thermodynamics of phase equilibria in scalar active matter. *Phys. Rev. E* **97**, 020602 (2018).
48. Solon, A. P., Stenhammar, J., Cates, M. E., Kafri, Y. & Tailleur, J. Generalized thermodynamics of motility-induced phase separation: phase equilibria, Laplace pressure, and change of ensembles. *New J. Phys.* **20**, 075001 (2018).
49. Marchetti, M. C. *et al.* Hydrodynamics of soft active matter. *Rev. Mod. Phys.* **85**, 1143–1189 (2013).
50. Hagan, M. F. & Baskaran, A. Emergent self-organization in active materials. *Curr. Opin. Cell Biol.* **38**, 74–80 (2016).
51. Fodor, É. & Marchetti, M. C. The statistical physics of active matter: From self-catalytic colloids to living cells. *Physica A* **504**, 106–120 (2018).
52. Shaebani, M. R., Wysocki, A., Winkler, R. G., Gompper, G. & Rieger, H. Computational models for active matter. *Nat. Rev. Phys.* **2**, 181–199 (2020).
53. Jones, T. B. *Electromechanics of Particles* (Cambridge University Press, 1995).
54. Zwanzig, R. *Nonequilibrium Statistical Mechanics* (Oxford University Press, New York, 2001).
55. Mazo, R. M. *Brownian Motion. Fluctuations, Dynamics, and Applications* (Oxford University Press, 2002).
56. Balescu, R. *Equilibrium and Nonequilibrium Statistical Mechanics* (John Wiley & Sons, 1975).
57. Le Bellac, M., Mortessagne, F. & Batrouni, G. G. *Equilibrium and Non-Equilibrium Statistical Thermodynamics* (Cambridge University Press, 2004).

58. Härtel, A., Richard, D. & Speck, T. Three-body correlations and conditional forces in suspensions of active hard disks. *Phys. Rev. E* **97**, 012606 (2018).
59. Solon, A. P. *et al.* Pressure and Phase Equilibria in Interacting Active Brownian Spheres. *Phys. Rev. Lett.* **114**, 198301 (2015).

METHODS

Particle synthesis

Following protocols described elsewhere³⁴, a submonolayer of 3 μm -diameter silica particles (Tokuyama) is prepared on a standard glass slide. To obtain metal-dielectric Janus particles, 20 nm of titanium and then 5 nm of SiO_2 are deposited vertically on the glass slide using an electron-beam evaporator. The preparation is then washed with isopropyl alcohol and deionized water, and then sonicated into deionized water to collect the Janus particles.

Experimental setup

NaCl stock solution is added to the particle suspension to obtain 0.05 mM NaCl solutions. The particle suspensions are confined between two coverslips (SPI Supplies) coated with indium tin oxide to make them conductive, and with 25 nm of silicon oxide to prevent particles from sticking to them. The coverslips have a 9 mm hole in the center, separated by a 120 μm -thick spacer (GraceBio SecureSeal). An alternating voltage is applied between the coverslips using a function generator (Agilent 33522A). The sample cell is imaged with 5X and 40X air objectives on an inverted microscope (Axiovert 200). Microscopic images and videos are taken with a CMOS camera (Edmund Optics 5012M GigE) with 20 ms time resolution.

Image analysis

Image processing is performed using MATLAB with home-developed codes, which are available upon request to the corresponding author.

Supplementary Information

SUPPLEMENTARY FIGURES

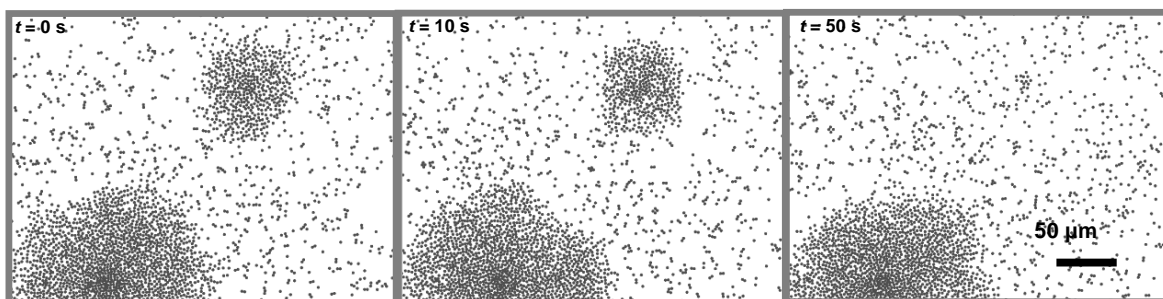


Figure S1 | Ostwald ripening of active colloids. Series of snapshots showing a small cluster shrinking and disappearing as part of the coarsening process.

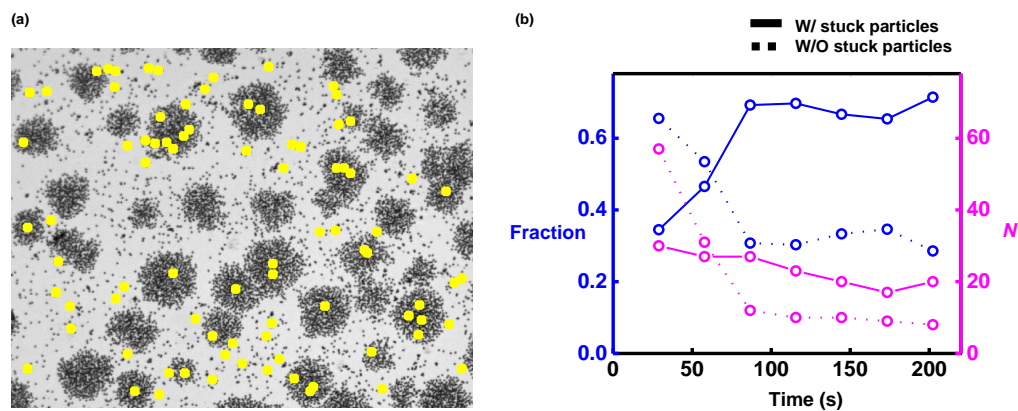


Figure S2 | Clusters with and without stuck particles. **a**, A bright field microscopy image of active phase separation in a late stage with yellow stars labelling particles that, stuck to the coverslip, remain in the same location throughout the experiment. **b**, The number (magenta) and fraction (blue) of clusters with and without (solid and dotted curves, respectively) at least one stuck particle. In the beginning of the experiment, more clusters are formed without than with stuck particles. With elapsed time, the number of clusters forming both with and without stuck particles decreases (magenta), but clusters with stuck particles become the most abundant.

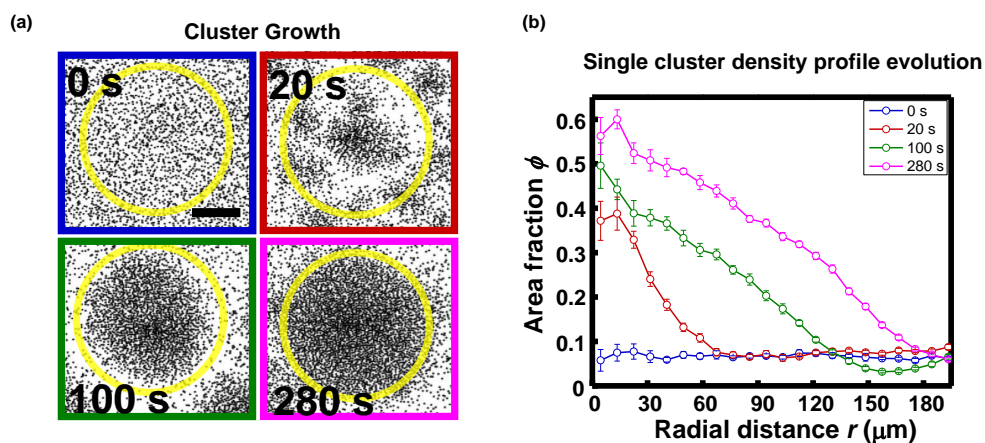


Figure S3 | Dynamics of cluster growth. **a**, Snapshots of cluster growth upon AC electric field application ([Movie 2](#)). Scale bar, $100 \mu\text{m}$. The yellow circumference indicates the outline of the cluster in the final snapshot. **b**, Density profile evolution in the growing cluster shown in **a**. Averages are over 20 frames (1.2 s) centered at each designated time point. Error bars are S.D.

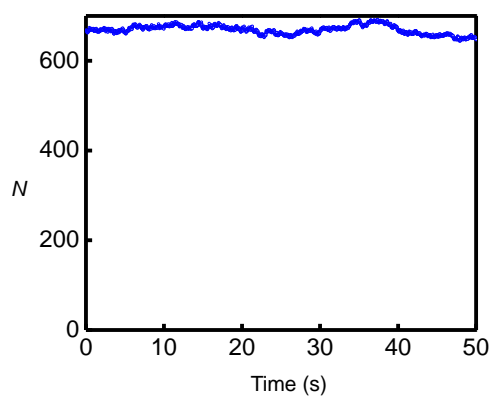


Figure S4 | Particle-number fluctuations in a quasi-steady state cluster. The number of particles in this cluster, the same cluster also shown in [Figs. 1](#) and [2](#), remains roughly constant during the time when averages are taken.

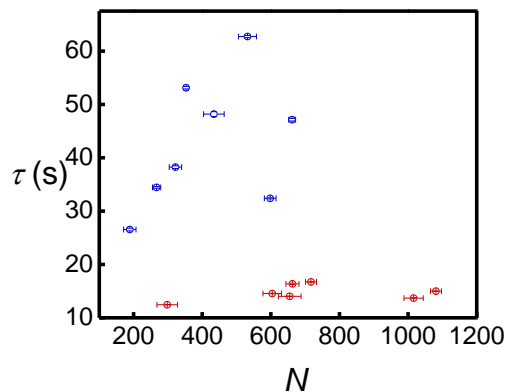


Figure S5 | Particle turnover time depends on cluster size and particle speed. The turnover time τ , defined in Fig. 2b, depends on the number of particles N in the cluster, and on particle speed and interactions. The number of particles is averaged over the time used to calculate the turnover time τ as in Fig. 2b. This averaging time varies from 30 to 180 s in different clusters. Error bars are S.D. Blue points correspond to an applied electric field with amplitude 66 V/mm and frequency 30 kHz, producing an average single-particle speed of $12 \mu\text{m/s}$ within clusters. Red points correspond to a field with the same frequency but amplitude 83 V/mm, giving an average single-particle speed of $22 \mu\text{m/s}$ within clusters. Particles with higher speeds and stronger interactions turn over more quickly.

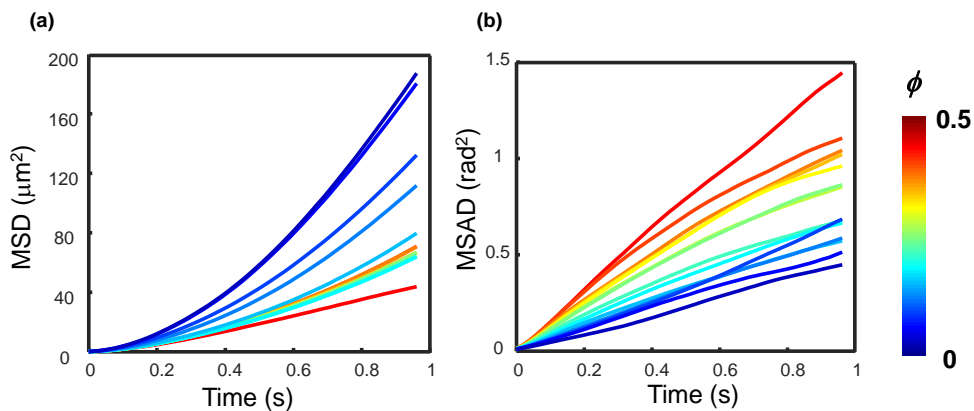


Figure S6 | Mean square displacements. Mean square displacements of particle position (a) and angle (b) for particles at different local area fractions ϕ . The particle speed and effective rotational diffusivity shown in Fig. 2c are obtained from the first 0.5 s of these data by fitting $\text{MSD} = (vt)^2$ and $\text{MSAD} = D_r^{\text{eff}}t$, respectively.

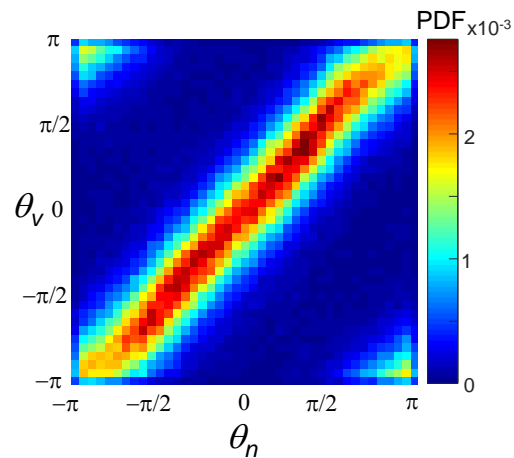


Figure S7 | Orientation-velocity coincidence prior to clustering. Joint probability distribution function (PDF) of the particle orientation and velocity angles, as defined in Fig. 3d, prior to cluster formation. In contrast to the mismatch found in clusters (Figs. 3e and 3f), the orientation and velocity directions coincide before clusters form.

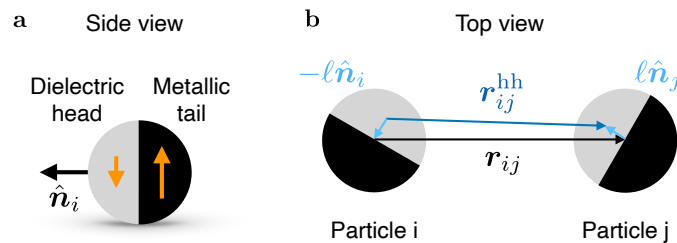


Figure S8 | Schematic of Janus particles' polarization and dipolar interactions. **a**, In the parameter regime used in the experiments, both hemispheres of the Janus particles polarize along the axis of the external electric field, parallel to the particle's equator. However, the metallic and dielectric hemispheres acquire effective dipolar moments of different magnitude and sign (orange arrows). The particles self-propel in a direction \hat{n}_i (black arrow), which points from the metallic tail to the dielectric head of the particles. **b**, The net interaction between two particles results from all the interactions between their off-centered head and tail dipoles. For example, the interaction between the dipoles in the head hemispheres of two particles depends on their distance vector $\mathbf{r}_{ij}^{\text{hh}}$ (dark blue arrow). The schematic shows how this vector is related to the center-of-mass distance vector \mathbf{r}_{ij} (black arrow): $\mathbf{r}_{ij}^{\text{hh}} = -\ell\hat{n}_i + \mathbf{r}_{ij} + \ell\hat{n}_j$. Light blue arrows represent the distance vector between the center of mass of the particles and the center of their head hemisphere.

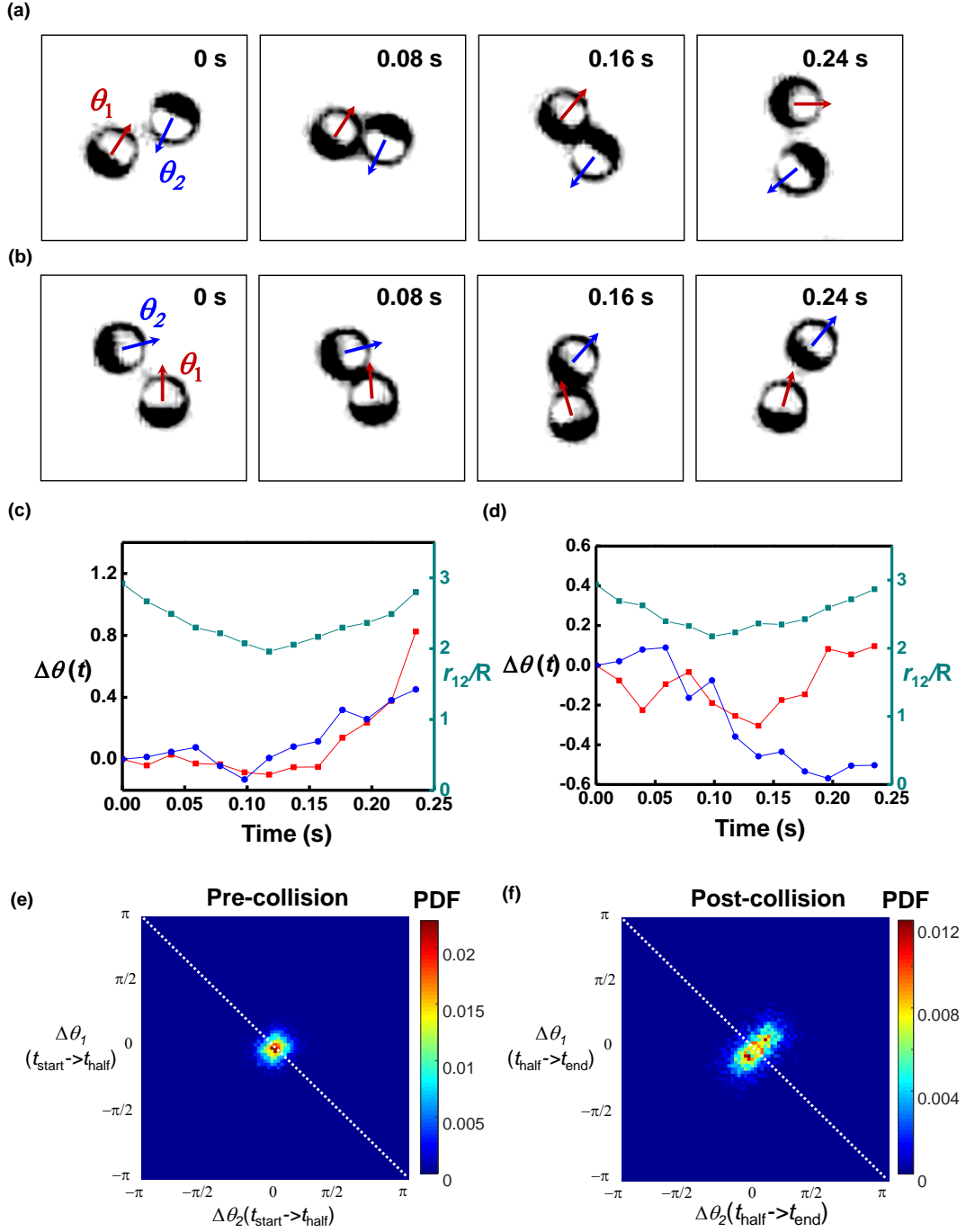


Figure S9 | Dynamics and statistics of two-particle interaction events. **a,b**, Two examples of interaction events between two particles, which we define by the condition $r_{12} < 3R$, with R the particle radius. We also require the minimal interparticle distance to be $\min r_{12} < 2.2R$. We analyzed 2061 of such interaction events. In **a**, both particles turn clockwise. Therefore, the interaction torque has the same sign on both particles, showing that torques are non-reciprocal ($\Gamma_{12} \neq -\Gamma_{21}$). This type of interaction with particles initially pointing in opposite directions, defined by the condition $|\theta_1(t=0) + \theta_2(t=0)| < 0.2$ rad, occurred in $\sim 33\%$ of the analyzed events. In **b**, particle 1 changes its orientation very little compared to particle 2, showing another example of non-reciprocal torques. The particles end up aligned in a chain. This type of interaction, defined by the condition $\min(\theta_1(t) - \theta_2(t)) < 0.5$ rad during the interaction event, occurred in $\sim 2.8\%$ of the analyzed events. **c,d**, Evolution of the interparticle distance, r_{12} , and the change in angle of each particle, $\Delta\theta_{1,2}$, for the interactions events in **a** and **b**, respectively. **e,f**, Joint probability distribution functions of the angle changes of each particle in an interacting pair. The pre-collision (**e**) and post-collision (**f**) phases respectively correspond to the times before and after the particles reach their minimal distance. These histograms show that, statistically, both particles in the interacting pair tend to turn in the same direction, showing that interaction torques are non-reciprocal. Reciprocal torques would lead to particles rotating in opposite directions and by the same magnitude, as indicated by the dashed lines.

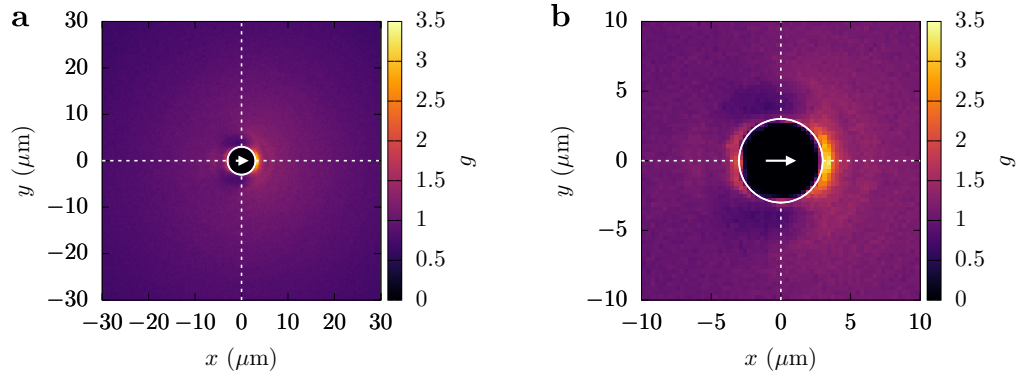


Figure S10 | Pair distribution function measured in experiments. **a**, Full $g(x, y)$ used in the calculation of the collective force and torque coefficients ζ_0 , ζ_1 , and τ_1 (see text and Eq. (S37)). **b**, Zoomed-in region, which allows to more clearly appreciate that the pair distribution function is anisotropic, indicating that it is more likely to find another particle in front than behind a reference self-propelled particle. In each panel, the arrow indicates the direction of self-propulsion of the reference particle, dashed lines indicate the coordinate axes, and the white circle indicates the region $r < 2R$ of volume exclusion between two particles.

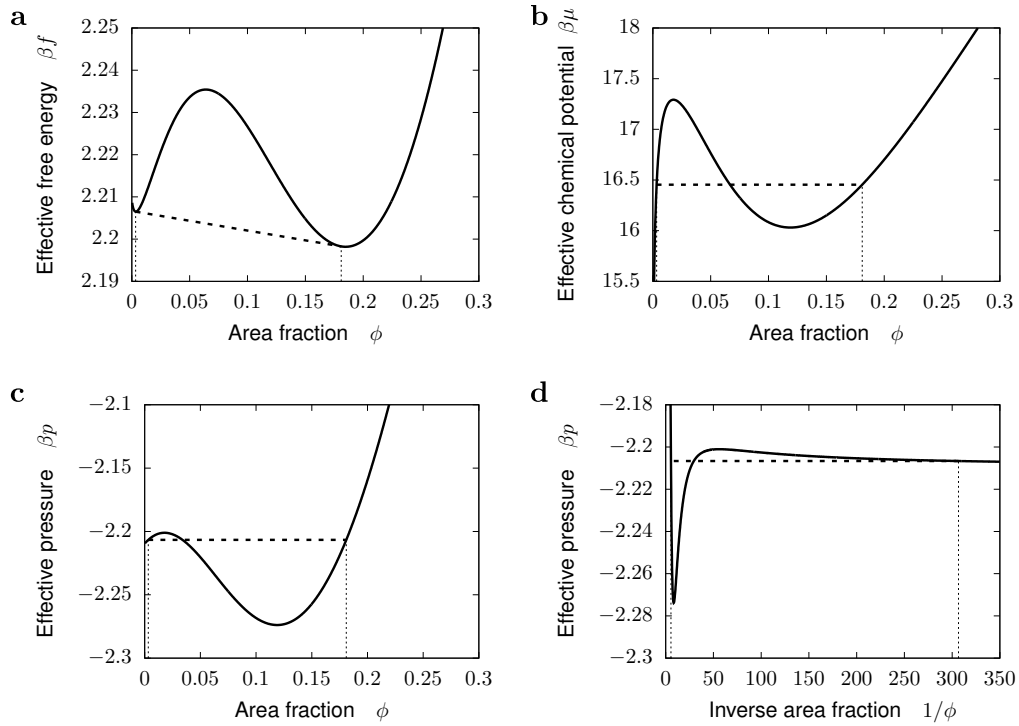


Figure S11 | Effective thermodynamics of torque-based MIPS. Effective free energy density (**a**, Eq. (S56)), chemical potential (**b**, Eq. (S55)), and thermodynamic pressure (**c-d**, Eq. (S57)) of the active Janus suspension as a function of the area fraction of particles, for $v_0 = 10 \mu\text{m/s}$. The remaining parameter values are evaluated using the estimates in Table I. To better visualize the double-well shape of the free energy $\beta f(\phi)$, we added a linear term -16.5ϕ , which does not affect phase coexistence. Thin dashed lines indicate the densities of the coexisting phases. These densities are obtained from the common-tangent construction on the free energy density (**a**), which corresponds to equality of both chemical potential (**b**) and pressure (**c**), as indicated by thick dashed lines. Alternatively, the common-tangent construction also corresponds to the Maxwell construction on the curve $p(1/\phi)$, as indicated by the thick dashed line in panel **d**.

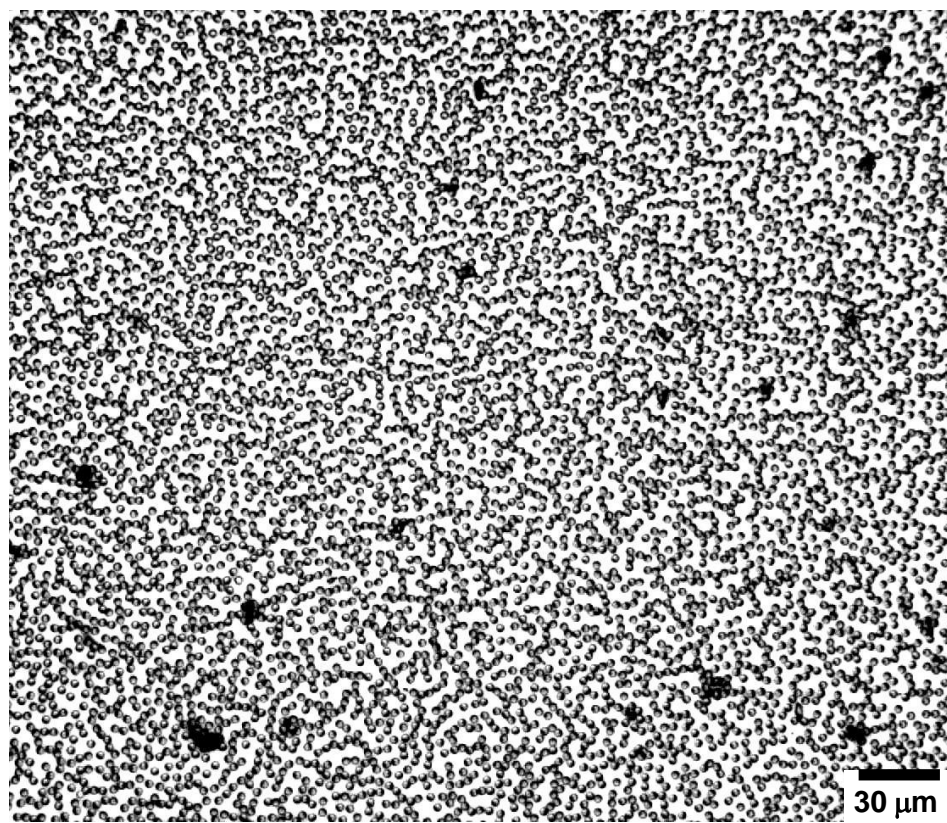


Figure S12 | High-density uniform phase. Snapshot of the uniform phase found at $\phi = 0.35$, showing transient particle chains throughout the system.

SUPPLEMENTARY MOVIES

Supplementary Movie 1: Coarsening dynamics during active phase separation. This movie, taken with a 5x objective, shows the phase separation process of a quasi-2D Janus particle system (area fraction $\phi \sim 0.12$) when AC electric field (30 kHz, 83 V/mm) perpendicular to the imaging plane is applied. The movie is played at 10x real speed.

Supplementary Movie 2: Growth of a representative active cluster. This movie, from which the snapshots in [Fig. S3](#) are taken, is obtained using a perpendicular AC electric field (30 kHz, 83 V/mm), and is played at 20x real speed.

Supplementary Movie 3: Particle turnover dynamics for an active cluster whose population remains nearly constant. The movie is taken after the perpendicular AC electric field (30 kHz, 67 V/mm) has been applied for a few minutes and the clusters are coarsening. Particles are color-coded according to their distance from the cluster centroid in the first frame, which is an arbitrary time point. Particles joining the cluster after the first frame are not labeled. This movie is played at 2x real speed and associated with [Fig. 2](#).

Supplementary Movie 4: Particle turnover dynamics for two clusters of different sizes. The plots on the right refer to the movies on the left. Native particles are defined as those particles within the frame at the beginning of the movie. $N_0(t)$ is the number of native particles remaining in the frame after time t . Both movies are taken after the perpendicular AC electric field (30 kHz, 67 V/mm) has been applied for a few minutes. Particles are color-coded according to their distance from the cluster centroid in the first frame, which is an arbitrary time point. Particles joining the cluster after the first frame are not labeled. This movie is played at 2x real speed.

Supplementary Movie 5: Flickering chains in an active cluster. Lines are drawn to connect pairs of particles whose centers are separated by less than $3R$ ($R = 1.5 \mu\text{m}$ is the particle radius), color-coded by the degree of pair alignment, with red indicating alignment and blue anti-alignment. This movie is played at 0.2x real speed. A snapshot of this movie is presented in [Fig. 3a](#).

Supplementary Movie 6: High-density uniform phase with transient particle chains. This movie, taken with a 20x objective, shows the high-density uniform phase (area fraction $\phi \sim 0.35$) with transient particle chains when AC electric field (30 kHz, 83 V/mm) perpendicular to the imaging plane is applied. A snapshot of this movie is presented in [Fig. S12](#).

SUPPLEMENTARY NOTE

In this Supplementary Note, we provide a detailed account of our theory for torque-based motility-induced phase separation. We start by proposing a simple microscopic model for the dynamics of self-propelled Janus colloids interacting via electrostatic forces. Because these forces are non-central, they lead to interparticle torques. We then systematically coarse-grain the microscopic equations of motion to obtain a hydrodynamic description in terms of continuum equations, which describe the collective behavior of the active colloids. This coarse-graining derivation shows how interparticle torques reorient particle motion toward regions with higher particle density. We then show that, when combined with particle self-propulsion, this reorientation produces a spinodal instability leading to phase separation. We predict the phase diagram, including the densities of the coexisting dense and dilute phases. Finally, we provide experimental estimates for the model parameters. Overall, we demonstrate a new mechanism for motility-induced phase separation (MIPS) that relies on interparticle torques instead of central forces. Thus, this torque-based MIPS mechanism is an alternative to the originally-proposed one, namely the slowdown of particle motion with increasing density due to repulsion between the particles^{1,5}.

A. Microscopic model: Active Janus particles with electrostatic interactions

1. Dielectric response and electrostatic interactions between Janus colloids

In our experiments, metal-dielectric Janus particles are driven by an alternating electric field. This field induces an electric polarization in each hemisphere of the Janus particles (Fig. S8a). Due both to Ohmic losses and to the Maxwell-Wagner effect produced by the metal coating on one of the hemispheres, the electric polarization has a delay with respect to the electric field⁵³. This dynamic response can be taken into account via a complex and frequency-dependent dielectric permittivity of the material

$$\bar{\epsilon}(\omega) = \epsilon - i \frac{\sigma}{\omega}, \quad (\text{S1})$$

where ϵ is the static dielectric permittivity, σ is the conductivity of the material, and ω is the angular frequency.

The electric polarization of the hemispheres results in electrostatic interactions between the particles. Here, we model these interactions as resulting from point dipoles located at the center of each hemisphere. Taking into account electrodynamic effects via the complex permittivity in Eq. (S1), the dipole moment induced by an alternating electric field with amplitude E_0 and frequency ν in a hemisphere of radius R with isotropic properties is given by⁵³

$$\mathbf{d}_c(\nu) = 2\pi\epsilon K(\nu)R^3 \mathbf{E}_0, \quad (\text{S2})$$

where the subscript c stands for complex. Here, $K(\nu)$ is the Clausius-Mossotti function that characterizes the frequency

dependence, which was previously measured for each hemisphere of our Janus particles³⁴.

In our particles, electric dipoles are either parallel or antiparallel to each other, and they are perpendicular to the particles' plane of motion (Fig. S8a). For this specific arrangement, the electrostatic force exerted by a complex point dipole a on another complex point dipole b is given by⁵³

$$\mathbf{F}_{ab} = \frac{3 \operatorname{Re}[\mathbf{d}_{c,a}^* \cdot \mathbf{d}_{c,b}]}{4\pi\epsilon r^4} \hat{\mathbf{r}}, \quad (\text{S3})$$

where $\mathbf{r} = \mathbf{r}_b - \mathbf{r}_a$ is the distance vector between the two dipoles, and $r = |\mathbf{r}|$. This interaction can be recast as

$$\mathbf{F}_{ab} = \frac{3\mathbf{d}_a \cdot \mathbf{d}_b}{4\pi\epsilon r^4} \hat{\mathbf{r}}, \quad (\text{S4})$$

where \mathbf{d}_a and \mathbf{d}_b are effective non-complex dipoles. The effective dipoles d_h and d_t of the head and tail hemispheres of our Janus particles, respectively, are

$$d_{h,t} = 2\pi\epsilon R^3 E_0 |K_{h,t}(\nu)|, \quad (\text{S5})$$

where $|K_{h,t}(\nu)| = \sqrt{\operatorname{Re}[K_{h,t}(\nu)]^2 + \operatorname{Im}[K_{h,t}(\nu)]^2}$ are the moduli of the complex numbers $K_{h,t}(\nu)$. Moreover, whereas the squares of the effective dipole moments are directly the d_h^2 and d_t^2 , the product $d_t d_h$ is given by

$$d_h d_t = (2\pi\epsilon R^3 E_0)^2 \operatorname{Re}[K_h^* K_t]. \quad (\text{S6})$$

With these substitutions, we can encode the dynamic dielectric response of the particles into effective dipole moments.

2. Electrostatic force and torque between Janus colloids

The dipole-dipole forces described by Eq. (S4) are isotropic and central. However, the dipoles are located at the center of each hemisphere, and not at the center of the particle (Fig. S8a). Moreover, the effective dipole in the metallic hemisphere (particle tail, d_t) is different in magnitude and sign than the dipole in the dielectric hemisphere (particle head, d_h). As a result, the dipolar forces on the head and tail hemispheres are different. Thus, the electrostatic interactions between two particles are non-central, and they produce not only a net force but also a net torque (Fig. 1b). We obtain both the net force and the net torque below.

For particle i , the dipoles of the head and tail hemispheres are respectively located at $\mathbf{r}_i^{h,t} = \pm \ell \hat{\mathbf{n}}_i$, where $\hat{\mathbf{n}}_i$ is the direction of self-propulsion, perpendicular to the equator (Fig. S8), and $\ell = 3R/8$ is the distance between the center of mass of the hemisphere and that of the particle. The total force exerted by particle i on particle j is the sum of four dipolar contributions (head-head, head-tail, tail-head, and tail-tail):

$$\mathbf{F}_{ij} = \mathbf{F}_{ij}^{hh} + \mathbf{F}_{ij}^{ht} + \mathbf{F}_{ij}^{th} + \mathbf{F}_{ij}^{tt}. \quad (\text{S7})$$

Each term involves its own dipolar moments and distance vector. The head and tail dipolar moments are $\mathbf{d}_h = d_h \hat{\mathbf{z}}$ and $\mathbf{d}_t = d_t \hat{\mathbf{z}}$, with $d_t > 0$, $d_h < 0$, and $d_t > |d_h|$ (Fig. S8a). Respectively, the distance vectors for each contribution can be

written in terms of the distance vector \mathbf{r}_{ij} between the particles' centers of mass and their individual self-propulsion directions $\hat{\mathbf{n}}_i$ and $\hat{\mathbf{n}}_j$. Performing the vector sums illustrated in Fig. S8b, the distance vectors for each dipolar interaction are

$$\mathbf{r}_{ij}^{\text{hh}} = -\ell\hat{\mathbf{n}}_i + \mathbf{r}_{ij} + \ell\hat{\mathbf{n}}_j, \quad (\text{S8a})$$

$$\mathbf{r}_{ij}^{\text{ht}} = -\ell\hat{\mathbf{n}}_i + \mathbf{r}_{ij} - \ell\hat{\mathbf{n}}_j, \quad (\text{S8b})$$

$$\mathbf{r}_{ij}^{\text{th}} = \ell\hat{\mathbf{n}}_i + \mathbf{r}_{ij} + \ell\hat{\mathbf{n}}_j, \quad (\text{S8c})$$

$$\mathbf{r}_{ij}^{\text{tt}} = \ell\hat{\mathbf{n}}_i + \mathbf{r}_{ij} - \ell\hat{\mathbf{n}}_j. \quad (\text{S8d})$$

In terms of these vectors, the net interparticle force is expressed as

$$\mathbf{F}_{ij} = \frac{3}{4\pi\epsilon} \left[\frac{d_h^2}{|\mathbf{r}_{ij}^{\text{hh}}|^4} \hat{\mathbf{r}}_{ij}^{\text{hh}} + \frac{d_h d_t}{|\mathbf{r}_{ij}^{\text{ht}}|^4} \hat{\mathbf{r}}_{ij}^{\text{ht}} + \frac{d_t d_h}{|\mathbf{r}_{ij}^{\text{th}}|^4} \hat{\mathbf{r}}_{ij}^{\text{th}} + \frac{d_t^2}{|\mathbf{r}_{ij}^{\text{tt}}|^4} \hat{\mathbf{r}}_{ij}^{\text{tt}} \right]. \quad (\text{S9})$$

Note that this force is non-central; in addition to a component along the interparticle distance axis $\hat{\mathbf{r}}_{ij}$, it has components along each particle's self-propulsion direction $\hat{\mathbf{n}}_i$ and $\hat{\mathbf{n}}_j$.

The off-centered dipolar interactions lead to torques. Like the net force, the total torque exerted by particle i on the center of mass of particle j also has four contributions:

$$\mathbf{\Gamma}_{ij} = \mathbf{r}_j^{\text{h}} \times (\mathbf{F}_{ij}^{\text{hh}} + \mathbf{F}_{ij}^{\text{th}}) + \mathbf{r}_j^{\text{t}} \times (\mathbf{F}_{ij}^{\text{ht}} + \mathbf{F}_{ij}^{\text{tt}}). \quad (\text{S10})$$

Using the distance vectors between the head and tail hemispheres, the center-of-mass torque can be expressed as

$$\begin{aligned} \mathbf{\Gamma}_{ij} = & \frac{3\ell}{4\pi\epsilon} \left[\left(\frac{d_h^2}{|\mathbf{r}_{ij}^{\text{hh}}|^5} + \frac{d_t d_h}{|\mathbf{r}_{ij}^{\text{th}}|^5} - \frac{d_h d_t}{|\mathbf{r}_{ij}^{\text{ht}}|^5} - \frac{d_t^2}{|\mathbf{r}_{ij}^{\text{tt}}|^5} \right) \hat{\mathbf{n}}_j \times \mathbf{r}_{ij} \right. \\ & \left. + \left(-\frac{d_h^2}{|\mathbf{r}_{ij}^{\text{hh}}|^5} + \frac{d_t d_h}{|\mathbf{r}_{ij}^{\text{th}}|^5} + \frac{d_h d_t}{|\mathbf{r}_{ij}^{\text{ht}}|^5} - \frac{d_t^2}{|\mathbf{r}_{ij}^{\text{tt}}|^5} \right) \ell \hat{\mathbf{n}}_j \times \hat{\mathbf{n}}_i \right]. \end{aligned} \quad (\text{S11})$$

Similar to the net force, the center-of-mass torque has a term involving the interparticle distance vector $\hat{\mathbf{r}}_{ij}$ but also a term associated entirely with the particles' self-propulsion direction, $\hat{\mathbf{n}}_i$ and $\hat{\mathbf{n}}_j$.

Throughout most of the experiments, and certainly in the initial condition, the interparticle distance r_{ij} is typically much larger than the distance $\ell \approx 0.5 \mu\text{m}$ between the center of mass of the particle and of either hemisphere, $r_{ij} \gg \ell$. We leverage this condition to obtain simpler expressions for the interparticle force and torque. Expanding Eqs. (S10) and (S11) to lowest order in ℓ/r_{ij} , we obtain

$$\mathbf{F}_{ij} \approx \frac{3}{4\pi\epsilon} \frac{(d_h + d_t)^2}{r_{ij}^4} \hat{\mathbf{r}}_{ij}, \quad (\text{S12})$$

$$\mathbf{\Gamma}_{ij} \approx \frac{3\ell}{4\pi\epsilon} \frac{d_h^2 - d_t^2}{r_{ij}^4} \hat{\mathbf{n}}_j \times \hat{\mathbf{r}}_{ij}. \quad (\text{S13})$$

At this level of approximation, the net interparticle force \mathbf{F}_{ij} is central (i.e., along $\hat{\mathbf{r}}_{ij}$). Respectively, given that $d_t^2 > d_h^2$,

the net interparticle torque $\mathbf{\Gamma}_{ij}$ tends to rotate particles toward the direction of the interparticle distance (Fig. 1b).

Finally, the electrodes that generate the electric field are equipotential surfaces. Therefore, they screen the electrostatic interactions between particles over a length scale comparable to the distance between electrodes, $\lambda = 120 \mu\text{m}$ (Fig. 1a). Without solving the full electrostatic problem in detail, we account for screening effects by adding an exponential factor $e^{-r_{ij}/\lambda}$. Thus, the final expressions of the interparticle force and torque are

$$\mathbf{F}_{ij} \approx \frac{3}{4\pi\epsilon} \frac{(d_h + d_t)^2}{r_{ij}^4} e^{-r_{ij}/\lambda} \hat{\mathbf{r}}_{ij}, \quad (\text{S14a})$$

$$\mathbf{\Gamma}_{ij} \approx \frac{3\ell}{4\pi\epsilon} \frac{d_h^2 - d_t^2}{r_{ij}^4} e^{-r_{ij}/\lambda} \hat{\mathbf{n}}_j \times \hat{\mathbf{r}}_{ij}. \quad (\text{S14b})$$

3. Langevin equations of motion

Upon the application of an electric field, our metal-dielectric Janus particles become self-propelled by virtue of induced-charge electrophoresis^{32,33}. Therefore, in addition to the interaction force and torque in Eq. (S14), our Janus particles are driven by self-propulsion forces, as well as both translational and rotational fluctuations. These driving forces are balanced by damping forces in the form of viscous friction between the particles and the solvent. Hydrodynamic interactions between particles are negligible in front of electrostatic interactions³⁴. Putting all together, we can write the Langevin equations for the translational and rotational motion of particle i as

$$\frac{d\mathbf{r}_i}{dt} = v_0 \hat{\mathbf{n}}_i + \frac{\mathbf{F}_i}{\xi_t} + \boldsymbol{\eta}_i^t(t); \quad \mathbf{F}_i = \sum_{j \neq i} \mathbf{F}_{ji}, \quad (\text{S15a})$$

$$\frac{d\hat{\mathbf{n}}_i}{dt} = \frac{\mathbf{\Gamma}_i}{\xi_r} + \boldsymbol{\eta}_i^r(t); \quad \mathbf{\Gamma}_i = \sum_{j \neq i} \mathbf{\Gamma}_{ji}. \quad (\text{S15b})$$

Here, v_0 is the self-propulsion speed, and ξ_t and ξ_r are the translational and rotational friction coefficients, respectively, which we assume to be isotropic. Finally, $\boldsymbol{\eta}_i^t(t)$ and $\boldsymbol{\eta}_i^r(t)$ are respectively translational and rotational Gaussian white noises with zero mean and correlations given by

$$\langle \eta_{i,\alpha}^t(t) \eta_{j,\beta}^t(t') \rangle = 2D_t \delta_{ij} \delta_{\alpha\beta} \delta(t - t'), \quad (\text{S16a})$$

$$\langle \eta_{i,\alpha}^r(t) \eta_{j,\beta}^r(t') \rangle = 2D_r \delta_{ij} \delta_{\alpha\beta} \delta(t - t'). \quad (\text{S16b})$$

Here, Greek indices indicate spatial components. Respectively, D_t and D_r are the bare translational and rotational diffusion coefficients of the particles (in the absence of self-propulsion), which, as for the friction coefficients, we assume to be isotropic.

4. Torque on the common center of mass of two particles

Before proceeding to coarse-grain this microscopic model, we note that the interaction torques $\mathbf{\Gamma}_{ij}$ are non-reciprocal,

i.e. $\Gamma_{ij} \neq -\Gamma_{ji}$. These torques act on the center of mass of each particle in the interacting pair, affecting particle orientation. To ensure overall torque balance, these interaction torques combine with the relative torque Γ_{rel} of the particles with respect to their common center of mass, located halfway between the two particles. To obtain Γ_{rel} , we obtain the corresponding angular momentum:

$$\mathbf{L}_{\text{rel}} = m \frac{\mathbf{r}_{ij}}{2} \times \mathbf{v}_j + m \frac{\mathbf{r}_{ji}}{2} \times \mathbf{v}_j = \frac{m}{2} \mathbf{r}_{ij} \times (\mathbf{v}_j - \mathbf{v}_i), \quad (\text{S17})$$

where m is the particle mass. Ignoring noise, we introduce the particle velocities using Eq. (S15a) to obtain

$$\mathbf{L}_{\text{rel}} = \frac{m}{2} v_0 \mathbf{r}_{ij} \times (\hat{\mathbf{n}}_j - \hat{\mathbf{n}}_i). \quad (\text{S18})$$

We then obtain the relative torque as

$$\begin{aligned} \Gamma_{\text{rel}} = \frac{d\mathbf{L}_{\text{rel}}}{dt} = \frac{m}{2} v_0 \left[(\mathbf{v}_j - \mathbf{v}_i) \times (\hat{\mathbf{n}}_j - \hat{\mathbf{n}}_i) \right. \\ \left. + \mathbf{r}_{ij} \times \left(\frac{d\hat{\mathbf{n}}_j}{dt} - \frac{d\hat{\mathbf{n}}_i}{dt} \right) \right]. \quad (\text{S19}) \end{aligned}$$

Using Eq. (S15), ignoring noise, we obtain

$$\Gamma_{\text{rel}} = m v_0 \left[\frac{1}{\xi_t} \mathbf{F}_{ij} \times (\hat{\mathbf{n}}_j - \hat{\mathbf{n}}_i) + \frac{1}{2\xi_r} \mathbf{r}_{ij} \times (\Gamma_{ij} - \Gamma_{ji}) \right], \quad (\text{S20})$$

where we have used that interaction forces are reciprocal but torques are not.

B. Coarse-graining: From the microscopic model to a hydrodynamic description

In this section, we systematically coarse-grain the microscopic equations of motion Eq. (S15) to derive hydrodynamic equations that capture the collective behavior of the active Janus particle suspension. To this end, we use standard methods of non-equilibrium statistical mechanics⁵⁴⁻⁵⁷, performing the derivation in steps:

1. We go from the Langevin equations of motion for the set of N interacting particles to the Smoluchowski equation, which describes the evolution of the system in terms of the N -particle distribution function. We then project the Smoluchowski equation onto particle coordinates to obtain the Bogoliubov-Born-Green-Kirkwood-Yvon (BBGKY) hierarchy of equations for the 1,2,3,...-particle distribution functions. We truncate this hierarchy at the 2-particle order. In this way, information about pair correlations becomes encoded into two interaction integrals known as the collective force and torque, respectively^{5,36,37}.
2. We perform a gradient expansion to obtain the collective force and torque in terms of the particle density field and its gradient.

3. We define continuum fields as moments of the one-particle distribution function, and obtain a hierarchy of hydrodynamic equations for these fields. Finally, we truncate the hierarchy at second order to obtain closed hydrodynamic equations to describe the large-scale behavior of our system.

We provide the details for each of these steps in separate subsections below.

1. Smoluchowski equation and BBGKY hierarchy

The behavior of the system encoded in the set of coupled Langevin equations Eq. (S15) can be equivalently described by the Smoluchowski equation, i.e. the Fokker-Planck equation for the N -particle distribution function $\Psi_N(\mathbf{r}_1, \hat{\mathbf{n}}_1, \dots, \mathbf{r}_N, \hat{\mathbf{n}}_N; t)$:

$$\partial_t \Psi_N = - \sum_{i=1}^N [\nabla_i \cdot \mathbf{J}_{t,i} + \hat{\mathbf{n}}_i \times \partial_{\hat{\mathbf{n}}_i} \cdot \mathbf{J}_{r,i}]. \quad (\text{S21})$$

Here, $\hat{\mathbf{n}} \times \partial_{\hat{\mathbf{n}}}$ is the rotation operator⁴⁹, and \mathbf{J}_t and \mathbf{J}_r are the translational and rotational probability currents, respectively, given by

$$\mathbf{J}_{t,i} = \left[v_0 \hat{\mathbf{n}}_i + \frac{\mathbf{F}_i}{\xi_t} \right] \Psi_N - D_t \nabla_i \Psi_N, \quad (\text{S22a})$$

$$\mathbf{J}_{r,i} = \frac{\Gamma_i}{\xi_r} \Psi_N - D_r \hat{\mathbf{n}}_i \times \partial_{\hat{\mathbf{n}}_i} \Psi_N. \quad (\text{S22b})$$

Hereafter, we describe the two-dimensional particle orientation $\hat{\mathbf{n}}_i$ in terms of the angle θ_i : $\hat{\mathbf{n}}_i = (\cos \theta_i, \sin \theta_i)^T$.

Next, we obtain the BBGKY hierarchy of equations for the distribution functions of increasing order. The distribution function of order k is defined as

$$\begin{aligned} \Psi_k(\mathbf{r}_1, \theta_1, \dots, \mathbf{r}_k, \theta_k; t) \equiv \frac{N!}{(N-k)!} \int d^2 \mathbf{r}_{k+1} \dots d^2 \mathbf{r}_N \\ \times \int d\theta_{k+1} \dots d\theta_N \Psi_N(\mathbf{r}_1, \theta_1, \dots, \mathbf{r}_N, \theta_N; t). \quad (\text{S23}) \end{aligned}$$

We start with the one-particle distribution function $\Psi_1(\mathbf{r}_1, \theta_1; t)$, which is the probability density of finding one particle (tagged with label 1) at position \mathbf{r}_1 , with orientation θ_1 , at time t , regardless of the positions and orientations of the other $N-1$ particles. Projecting Eq. (S21) according to the definition in Eq. (S23) for $k=1$, we obtain

$$\begin{aligned} \partial_t \Psi_1 = - \nabla_1 \cdot [(v_0 \hat{\mathbf{n}}_1 - D_t \nabla_1) \Psi_1] - \nabla_1 \cdot \frac{\mathbf{F}_{\text{int}}}{\xi_t} \\ - \partial_{\theta_1} \frac{\hat{\mathbf{z}} \cdot \Gamma_{\text{int}}}{\xi_r} + D_r \partial_{\theta_1}^2 \Psi_1. \quad (\text{S24}) \end{aligned}$$

Here, \mathbf{F}_{int} and Γ_{int} are the collective force and torque, respectively, which encode the effects of interactions on the tagged

particle. For pair-wise interactions, these collective quantities can be expressed in terms of the two-particle distribution function $\Psi_2(\mathbf{r}_1, \theta_1, \mathbf{r}_2, \theta_2; t)$ as

$$\begin{aligned} \mathbf{F}_{\text{int}}(\mathbf{r}_1, \theta_1; t) = & \\ & - \int d^2\mathbf{r}' F(|\mathbf{r}' - \mathbf{r}_1|) \frac{\mathbf{r}' - \mathbf{r}_1}{|\mathbf{r}' - \mathbf{r}_1|} \Psi_2(\mathbf{r}_1, \theta_1, \mathbf{r}'; t), \end{aligned} \quad (\text{S25a})$$

$$\begin{aligned} \Gamma_{\text{int}}(\mathbf{r}_1, \theta_1; t) = & \\ & \int d^2\mathbf{r}' \Gamma(|\mathbf{r}' - \mathbf{r}_1|) \hat{\mathbf{n}}_1 \times \frac{\mathbf{r}' - \mathbf{r}_1}{|\mathbf{r}' - \mathbf{r}_1|} \Psi_2(\mathbf{r}_1, \theta_1, \mathbf{r}'; t), \end{aligned} \quad (\text{S25b})$$

where we have already integrated over the orientation θ_2 of particle 2. Here,

$$F(r) = \frac{3(d_h + d_t)^2 e^{-r/\lambda}}{4\pi\epsilon r^4}, \quad (\text{S26a})$$

$$\Gamma(r) = \frac{3\ell(d_h^2 - d_t^2) e^{-r/\lambda}}{4\pi\epsilon r^4} \quad (\text{S26b})$$

are the scalar magnitudes of the interaction force and torque fields, as obtained from Eq. (S14).

With the collective force and torque given by Eq. (S25), Eq. (S24) is an integro-differential equation for Ψ_1 that involves Ψ_2 . Therefore, Eq. (S24) is the first equation in the BBGKY hierarchy. The simplest approximation to truncate this hierarchy is Boltzmann's molecular-chaos approximation, whereby pair correlations are ignored and Ψ_2 is expressed in terms of Ψ_1 . In active matter, however, pair correlations are crucial to capture the density-induced slowdown of particle motion, which is the original mechanism for motility-induced phase separation^{5,11}. We thus go beyond the molecular-chaos approximation and account for pair correlations. To do this, one should derive an integro-differential equation for Ψ_2 , which would involve Ψ_3 , and truncate the hierarchy at that level to obtain a closed expression for Ψ_2 ⁵⁸. Here, however, instead of obtaining Ψ_2 from its own equation in the hierarchy, we directly measure the pair correlation function in experiments (Fig. S10 and SI Section D) and use it as an input for the theory.

Specifically, to express Eq. (S24) as a closed equation for Ψ_1 , we decompose Ψ_2 as

$$\Psi_2(\mathbf{r}_1, \theta_1, \mathbf{r}'; t) = \rho(\mathbf{r}') g(\mathbf{r}' | \mathbf{r}_1, \theta_1; t) \Psi_1(\mathbf{r}_1, \theta_1; t). \quad (\text{S27})$$

Here, $\Psi_2(\mathbf{r}_1, \theta_1, \mathbf{r}'; t)$ is the density of particle pairs with one particle at position \mathbf{r}_1 with orientation θ_1 and another particle at position \mathbf{r}' with any orientation. Respectively, ρ is the density field, and g is the conventional dimensionless pair distribution function, so that $\rho(\mathbf{r}') g(\mathbf{r}' | \mathbf{r}_1, \theta_1)$ is the conditional density of particles at position \mathbf{r}' given that another particle is at position \mathbf{r}_1 with orientation θ_1 . Finally, $\Psi_1(\mathbf{r}_1, \theta_1)$ is the density of particles at position \mathbf{r}_1 with orientation θ_1 . Next, we express g in terms of the distance $|\mathbf{r}' - \mathbf{r}_1|$ between particles and the angle φ formed between the vector $\mathbf{r}' - \mathbf{r}_1$ that joins both particle centers and the orientation vector $\hat{\mathbf{n}}_1$ of particle 1:

$$\hat{\mathbf{n}}_1 \cdot \frac{\mathbf{r}' - \mathbf{r}_1}{|\mathbf{r}' - \mathbf{r}_1|} = \cos \varphi. \quad (\text{S28})$$

Moreover, we assume that pair correlations depend only on the relative coordinates of the particle pair, i.e. their distance $|\mathbf{r}' - \mathbf{r}_1|$ and angle φ , and not on the coordinates \mathbf{r}_1, θ_1 of the tagged particle 1. This assumption is verified in homogeneous states, and is therefore valid when we study the stability of the uniform isotropic state of the active Janus particle suspension. Finally, we focus on steady states, such that probability distributions are time-independent, and we drop the time variable hereafter. Mathematically, our assumptions read

$$g(\mathbf{r}' | \mathbf{r}_1, \theta_1) = g(|\mathbf{r}' - \mathbf{r}_1|, \varphi | \mathbf{r}_1, \theta_1) = g(|\mathbf{r}' - \mathbf{r}_1|, \varphi). \quad (\text{S29})$$

With this decomposition of the two-particle distribution function Ψ_2 , the collective force and torque (Eq. (S25)) are expressed as

$$\begin{aligned} \mathbf{F}_{\text{int}}(\mathbf{r}_1, \theta_1) = & -\Psi_1(\mathbf{r}_1, \theta_1) \\ & \times \int d^2\mathbf{r}' F(|\mathbf{r}' - \mathbf{r}_1|) \frac{\mathbf{r}' - \mathbf{r}_1}{|\mathbf{r}' - \mathbf{r}_1|} \rho(\mathbf{r}') g(|\mathbf{r}' - \mathbf{r}_1|, \varphi), \end{aligned} \quad (\text{S30a})$$

$$\begin{aligned} \Gamma_{\text{int}}(\mathbf{r}_1, \theta_1) = & \Psi_1(\mathbf{r}_1, \theta_1) \\ & \times \int d^2\mathbf{r}' \Gamma(|\mathbf{r}' - \mathbf{r}_1|) \hat{\mathbf{n}}_1 \times \frac{\mathbf{r}' - \mathbf{r}_1}{|\mathbf{r}' - \mathbf{r}_1|} \rho(\mathbf{r}') g(|\mathbf{r}' - \mathbf{r}_1|, \varphi). \end{aligned} \quad (\text{S30b})$$

2. Gradient expansion. Density-dependent collective force and torque

Via Eq. (S30), the collective force and torque depend non-locally on the density field $\rho(\mathbf{r}')$. To derive local hydrodynamic equations, we perform a gradient expansion on the density field:

$$\rho(\mathbf{r}') \approx \rho(\mathbf{r}_1) + \nabla \rho(\mathbf{r}_1) \cdot (\mathbf{r}' - \mathbf{r}_1). \quad (\text{S31})$$

Based on this expansion, we first obtain the zeroth-order contribution in the density gradient to the collective force and torque. Introducing Eq. (S31) into Eq. (S30), and changing the integration variable to the relative position $\mathbf{r} \equiv \mathbf{r}' - \mathbf{r}_1$, the zeroth-order term gives

$$\begin{aligned} \mathbf{F}_{\text{int}}^{(0)}(\mathbf{r}_1, \theta_1) = & -\Psi_1(\mathbf{r}_1, \theta_1) \rho(\mathbf{r}_1) \\ & \times \int_0^\infty dr r F(r) \int_0^{2\pi} d\varphi g(r, \varphi) \hat{\mathbf{r}}(\varphi), \end{aligned} \quad (\text{S32a})$$

$$\begin{aligned} \Gamma_{\text{int}}^{(0)}(\mathbf{r}_1, \theta_1) = & \Psi_1(\mathbf{r}_1, \theta_1) \rho(\mathbf{r}_1) \\ & \times \int_0^\infty dr r \Gamma(r) \int_0^{2\pi} d\varphi g(r, \varphi) \sin \varphi \hat{\mathbf{z}}, \end{aligned} \quad (\text{S32b})$$

where we have used that $\hat{\mathbf{n}}_1 \times \hat{\mathbf{r}} = \sin \varphi \hat{\mathbf{z}}$. For passive fluids with isotropic interactions, the pair distribution function is isotropic, $g(r, \varphi) = g(r)$. However, for active fluids, even with isotropic interactions, $g(r, \varphi)$ is anisotropic. This anisotropy is due to particle self-propulsion, which determines a direction and implies that other particles are more likely to be found in front than behind the tagged particle¹¹. In the absence of any chirality, $g(r, \varphi)$ is symmetric around the

particle self-propulsion axis, i.e. around $\varphi = 0$. Therefore, $g(r, \varphi)$ is an even function of φ . As a consequence, the component of the collective force $\mathbf{F}_{\text{int}}^{(0)}$ along the self-propulsion direction, $\mathbf{F}_{\text{int}}^{(0)} \cdot \hat{\mathbf{n}}_1$, is non-zero because $\hat{\mathbf{n}}_1 \cdot \hat{\mathbf{r}} = \cos \varphi$, and hence $g(r, \varphi) \cos \varphi$ is an even function of φ . In contrast, the component of the collective force perpendicular to the self-propulsion direction vanishes because $g(r, \varphi) \sin \varphi$ is an odd function of φ . For the same reason, the zeroth-order collective torque $\Gamma_{\text{int}}^{(0)}$ vanishes. Altogether:

$$\mathbf{F}_{\text{int}}^{(0)}(\mathbf{r}_1, \theta_1) = -\Psi_1(\mathbf{r}_1, \theta_1) \rho(\mathbf{r}_1) \hat{\mathbf{n}}_1 \times \int_0^\infty dr r F(r) \int_0^{2\pi} d\varphi g(r, \varphi) \cos \varphi, \quad (\text{S33a})$$

$$\Gamma_{\text{int}}^{(0)}(\mathbf{r}_1, \theta_1) = 0. \quad (\text{S33b})$$

$\Gamma_{\text{int}}^{(0)}$ corresponds to the collective torque experienced by a probe particle in a uniform-density background. Because interaction torques make particles orient toward the location of other particles (Eq. (S14b)), particles in a uniform density field have no preferred direction to orient toward. Therefore, the zeroth-order contribution to the collective torque vanishes.

Next, we obtain the first-order contribution in the density gradient to the collective force and torque. Using the same symmetry arguments as for the zeroth-order contribution, we obtain

$$\mathbf{F}_{\text{int},\parallel}^{(1)}(\mathbf{r}_1, \theta_1) = -\Psi_1(\mathbf{r}_1, \theta_1) \nabla_{\parallel} \rho(\mathbf{r}_1) \times \int_0^\infty dr r^2 F(r) \int_0^{2\pi} d\varphi g(r, \varphi) \cos^2 \varphi, \quad (\text{S34a})$$

$$\mathbf{F}_{\text{int},\perp}^{(1)}(\mathbf{r}_1, \theta_1) = -\Psi_1(\mathbf{r}_1, \theta_1) \nabla_{\perp} \rho(\mathbf{r}_1) \times \int_0^\infty dr r^2 F(r) \int_0^{2\pi} d\varphi g(r, \varphi) \sin^2 \varphi, \quad (\text{S34b})$$

for the force components parallel and perpendicular to the particle orientation $\hat{\mathbf{n}}_1$. The integrals in the parallel and perpendicular components are different. However, for typical forms of $g(r, \varphi)$, both integrals take similar values. Thus, to simplify the calculation, we ignore the small difference between these two integrals, replacing them by the average of both integrals. With this approximation, $\mathbf{F}_{\text{int}}^{(1)}$ is directly proportional to the density gradient. Respectively, for the collective torque, we obtain

$$\Gamma_{\text{int}}^{(1)}(\mathbf{r}_1, \theta_1) = \Psi_1(\mathbf{r}_1, \theta_1) \hat{\mathbf{n}}_1 \times \nabla \rho(\mathbf{r}_1) \times \int_0^\infty dr r^2 \Gamma(r) \int_0^{2\pi} d\varphi g(r, \varphi) \sin^2 \varphi. \quad (\text{S35})$$

Gathering the results for the zeroth- and first-order contributions, we finally have

$$\mathbf{F}_{\text{int}}(\mathbf{r}_1, \theta_1) \approx -\Psi_1(\mathbf{r}_1, \theta_1) [\zeta_0 \rho(\mathbf{r}_1) \hat{\mathbf{n}}_1 + \zeta_1 \nabla \rho(\mathbf{r}_1)], \quad (\text{S36a})$$

$$\Gamma_{\text{int}}(\mathbf{r}_1, \theta_1) = \Psi_1(\mathbf{r}_1, \theta_1) \tau_1 \hat{\mathbf{n}}_1 \times \nabla \rho(\mathbf{r}_1). \quad (\text{S36b})$$

Here, we have defined the coefficients

$$\zeta_0 \equiv \int_0^\infty dr r F(r) \int_0^{2\pi} d\varphi g(r, \varphi) \cos \varphi, \quad (\text{S37a})$$

$$\zeta_1 \equiv \frac{1}{2} \int_0^\infty dr r^2 F(r) \int_0^{2\pi} d\varphi g(r, \varphi), \quad (\text{S37b})$$

$$\tau_1 \equiv \int_0^\infty dr r^2 \Gamma(r) \int_0^{2\pi} d\varphi g(r, \varphi) \sin^2 \varphi, \quad (\text{S37c})$$

with $F(r)$ and $\Gamma(r)$ given in Eq. (S26). These coefficients capture the effects of interparticle interactions at the coarse-grained level, taking into account the anisotropy of the pair distribution function in systems of self-propelled particles. Specifically, the collective force and torque terms characterized by each of these coefficients (see Eq. (S36)) capture the following effects:

- *Repulsion-induced slowdown:* When the net central force between particles is repulsive ($F(r) > 0$), the term with $\zeta_0 > 0$ gives a force that opposes particle self-propulsion due to the higher probability of finding other particles in front than behind a given particle. The higher the particle density, the higher the opposing force. This opposing force causes the density-dependent slowdown of particle motion that is responsible for standard motility-induced phase separation^{1,5}.
- *Repulsion-induced diffusion:* For net repulsive interparticle forces ($F(r) > 0$), the term with $\zeta_1 > 0$ gives a force opposed to density gradients, tending to homogenize particle concentration like a diffusive flux.
- *Torque toward denser regions:* When the tail dipole has a larger magnitude than the head dipole, $d_t^2 > d_h^2$, we have $\Gamma(r) > 0$ (see Eq. (S26b)), and the term with τ_1 gives a torque that tends to align particle orientation $\hat{\mathbf{n}}_1$ with the density gradient, thus reorienting particle motion toward higher-density regions. Therefore, the collective torque Eq. (S36b) encodes the effect that is responsible for the new mechanism of motility-induced phase separation that we unveil here.

Whereas the repulsion-induced slowdown was obtained in previous studies^{5,11}, here we account both for repulsion-induced diffusion and, crucially, for torque toward denser regions by performing the gradient expansion up to first order in the density gradient.

To end this subsection, we introduce the final expressions for the collective force and torque (Eq. (S36)) into the Smoluchowski equation (Eq. (S24)) for the one-particle distribution function Ψ_1 . We obtain

$$\partial_t \Psi_1 = -\nabla \cdot \left\{ \left[\left(v_0 - \frac{\zeta_0}{\xi_t} \rho \right) \hat{\mathbf{n}} - \frac{\zeta_1}{\xi_t} \nabla \rho - D_t \nabla \right] \Psi_1 \right\} - \partial_\theta \left\{ \left[\frac{\tau_1}{\xi_r} \hat{\mathbf{z}} \cdot (\hat{\mathbf{n}} \times \nabla \rho) - D_t \partial_\theta \right] \Psi_1 \right\}. \quad (\text{S38})$$

Here, we have dropped the subscript 1 to indicate the tagged particle. We do that hereafter.

3. Torque non-reciprocity produces particle alignment toward denser regions

Before coarse-graining the model further, we note that the non-reciprocal character of the interaction torques (Eq. (S14b)), i.e. the fact that $\Gamma_{ij} \neq -\Gamma_{ji}$, is important for the reorientation of particles toward denser regions. Torques result from the electrostatic interactions between the dipoles in each hemisphere of the Janus particles. Therefore, the torque between particles i and j must be built based on three vectors: the distance vector \mathbf{r}_{ij} , and the self-propulsion direction of each particle, $\hat{\mathbf{n}}_i$ and $\hat{\mathbf{n}}_j$, which indicates the direction in which the dipoles are displaced from the particle's center of mass. Because the dipoles are perpendicular to the inter-particle distance, they only exert in-plane forces (Eq. (S4)). Hence, particles will rotate in their plane of motion, implying that the interaction torque points out of plane (along $\hat{\mathbf{z}}$). To build an out-of-plane vector from the three in-plane vectors \mathbf{r}_{ij} , $\hat{\mathbf{n}}_i$, and $\hat{\mathbf{n}}_j$, we must take vector products between them. Thus, the interaction torque could potentially be either $\Gamma_{ij} \propto \hat{\mathbf{n}}_i \times \hat{\mathbf{r}}_{ij}$, $\Gamma_{ij} \propto \hat{\mathbf{n}}_j \times \hat{\mathbf{r}}_{ij}$, or $\Gamma_{ij} \propto \hat{\mathbf{n}}_i \times \hat{\mathbf{n}}_j$.

The two first torques are non-reciprocal ($\Gamma_{ij} \neq -\Gamma_{ji}$); they orient one particle toward the location of the other particle. The third torque is reciprocal ($\Gamma_{ij} = -\Gamma_{ji}$); it tends to align the particles. Because this reciprocal torque does not depend on the direction in which the other particle is located, it cannot orient one particle toward the location of the other. Hence, reciprocal torques based on the electrostatic interactions in our system cannot reorient particles toward denser regions, and therefore they cannot lead to the torque-based phase separation that we report here. In other words, for reciprocal torques $\Gamma_{ij} \propto \hat{\mathbf{n}}_i \times \hat{\mathbf{n}}_j$, the collective torque Γ_{int} would vanish^{23,24}.

4. Moment hierarchy and hydrodynamic equations

To complete the coarse-graining of the microscopic model, we define continuum fields as the angular moments of the one-particle distribution function Ψ_1 . For example, the zeroth moment corresponds to the density field $\rho(\mathbf{r}, t)$, the first moment corresponds to the polarization density $\mathbf{p}(\mathbf{r}, t)$, and the second moment is related to the nematic order-parameter tensor density $\mathbf{Q}(\mathbf{r}, t)$:

$$\rho(\mathbf{r}, t) = \int \Psi_1(\mathbf{r}, \theta, t) d\theta, \quad (\text{S39a})$$

$$p_\alpha(\mathbf{r}, t) = \int n_\alpha \Psi_1(\mathbf{r}, \theta, t) d\theta, \quad (\text{S39b})$$

$$Q_{\alpha\beta}(\mathbf{r}, t) = \int \left[n_\alpha n_\beta - \frac{1}{2} \delta_{\alpha\beta} \right] \Psi_1(\mathbf{r}, \theta, t) d\theta. \quad (\text{S39c})$$

In general, the k^{th} moment of Ψ_1 with respect to the particle orientation $\hat{\mathbf{n}}$ corresponds to a k^{th} -rank orientational tensor field. We can then obtain hydrodynamic equations for each of these fields by taking the corresponding moment of the Smoluchowski equation Eq. (S38). Proceeding in this way, we obtain the following equations for the density and the po-

larity fields:

$$\partial_t \rho = -\nabla \cdot \left[\left(v_0 - \frac{\zeta_0}{\xi_t} \rho \right) \mathbf{p} \right] + \nabla \cdot \left(\frac{\zeta_1}{\xi_t} \rho \nabla \rho \right) + D_t \nabla^2 \rho, \quad (\text{S40a})$$

$$\begin{aligned} \partial_t \mathbf{p} = & -\nabla \cdot \left[\left(v_0 - \frac{\zeta_0}{\xi_t} \rho \right) \mathbf{Q} \right] - \frac{1}{2} \nabla \cdot \left[\left(v_0 - \frac{\zeta_0}{\xi_t} \rho \right) \rho \right] \\ & + \nabla \cdot \left(\frac{\zeta_1}{\xi_t} \mathbf{p} \nabla \rho \right) + D_t \nabla^2 \mathbf{p} \\ & - \frac{\tau_1}{\xi_r} \left(\mathbf{Q} \cdot \nabla \rho - \frac{1}{2} \rho \nabla \rho \right) - D_r \mathbf{p}. \end{aligned} \quad (\text{S40b})$$

In general, the equation for the k^{th} moment involves the $k+1^{\text{th}}$ moment, giving rise to a hierarchy of hydrodynamic equations.

To close this hierarchy, we eliminate the nematic tensor \mathbf{Q} in terms of the density and polarity fields. To this end, we obtain the equation for \mathbf{Q} :

$$\begin{aligned} \partial_t \mathbf{Q} = & \frac{v_0}{2} [-2\nabla \cdot \mathbf{T} - \mathbf{I}_3 \cdot \nabla \rho + \mathbf{I} \nabla \cdot \mathbf{p}] \\ & + \frac{\zeta_1}{\xi_t} \nabla \cdot [(\nabla \rho) \mathbf{Q}] + D_t \nabla^2 \mathbf{Q} - D_r \mathbf{Q} \\ & + \frac{\tau_1}{\xi_r} [(\nabla \rho) \mathbf{p} + \mathbf{p}(\nabla \rho) - 4\mathbf{T} \cdot \nabla \rho - 2\rho \mathbf{I}_3 \cdot \nabla \rho - \mathbf{I} \mathbf{p} \cdot \nabla \rho], \end{aligned} \quad (\text{S41})$$

where \mathbf{I}_3 is the third-rank identity tensor, and

$$T_{\alpha\beta\gamma}(\mathbf{r}, t) = \int \left[n_\alpha n_\beta n_\gamma - \frac{1}{2} \delta_{\alpha\beta\gamma} \right] \Psi_1(\mathbf{r}, \theta, t) d\theta \quad (\text{S42})$$

is the traceless third-rank tensor corresponding to the third-order orientational moment of Ψ_1 . A standard closure approximation then corresponds to setting $\mathbf{T} = \mathbf{0}$, and eliminating \mathbf{Q} by imposing $\partial_t \mathbf{Q} \approx \mathbf{0}$. This approximation is based on the fact that \mathbf{Q} relaxes faster than \mathbf{p} and ρ . Moreover, working in the hydrodynamic limit, we neglect terms with higher-order gradients of \mathbf{Q} in front of the relaxation term $2D_r \mathbf{Q}$. This way, \mathbf{Q} can be expressed in terms of the lower-order moments ρ and \mathbf{p} as

$$\begin{aligned} D_r \mathbf{Q} \approx & \frac{v_0}{2} [\mathbf{I} \nabla \cdot \mathbf{p} - \mathbf{I}_3 \cdot \nabla \rho] \\ & + \frac{\tau_1}{\xi_r} [(\nabla \rho) \mathbf{p} + \mathbf{p}(\nabla \rho) - 2\rho \mathbf{I}_3 \cdot \nabla \rho - \mathbf{I} \mathbf{p} \cdot \nabla \rho], \end{aligned} \quad (\text{S43})$$

and hence eliminated from Eq. (S40b). In practice, however, all the terms coming from \mathbf{Q} are of higher order in gradients than other terms in Eq. (S40b). Therefore, these \mathbf{Q} terms can be neglected in the hydrodynamic limit, which we focus on to predict the phase diagram of the system. Hence, for our practical purposes, we set $\mathbf{Q} = \mathbf{0}$. We then recast the hydro-

dynamic equations Eq. (S40) as

$$\partial_t \rho = -\nabla \cdot (v[\rho] \mathbf{p}) + \nabla \cdot ((D_t + D_{\text{rep}}[\rho]) \nabla \rho), \quad (\text{S44a})$$

$$\begin{aligned} \partial_t \mathbf{p} = & -D_r \mathbf{p} + D_t \nabla^2 \mathbf{p} - \frac{1}{2} \nabla (v[\rho] \rho) + \frac{1}{2} v_{\text{tor}}[\rho] \nabla \rho \\ & + \frac{D_{\text{rep}}[\rho]}{\rho} \nabla \cdot (\mathbf{p} \nabla \rho). \end{aligned} \quad (\text{S44b})$$

These equations explicitly showcase the effects of the different collective force and torque contributions at the hydrodynamic level. Specifically, the three effects listed in the previous subsection are encoded into three functionals,

$$v[\rho(\mathbf{r})] = v_0 - \zeta_0 \rho(\mathbf{r}) / \xi_t, \quad (\text{S45a})$$

$$D_{\text{rep}}[\rho(\mathbf{r})] = \zeta_1 \rho(\mathbf{r}) / \xi_t, \quad (\text{S45b})$$

$$v_{\text{tor}}[\rho(\mathbf{r})] = \tau_1 \rho(\mathbf{r}) / \xi_r, \quad (\text{S45c})$$

with the following interpretations:

- The repulsion-induced slowdown is apparent in the density-dependent particle speed $v[\rho]$ (Eq. (S45a)), which decreases with increasing density
- The repulsion-induced diffusion shows up as additional density-dependent diffusion coefficient $D_{\text{rep}}[\rho]$ (Eq. (S45b))
- The torque toward denser regions manifests as an additional density-dependent speed $v_{\text{tor}}[\rho]$ (Eq. (S45c)) for the polarity field, thus contributing to aligning polarity with the density gradient.

The coefficients ζ_0 , ζ_1 , and τ_1 that characterize each of these effects are given in Eq. (S37).

Equation (S44) are hydrodynamic equations for the coupled density and polarity fields of our suspension of interacting active particles. These equations are the final outcome of our derivation. Via the coarse-graining procedure presented in this section, we have obtained all the coefficients in Eq. (S44), which characterize the large-scale collective behavior of our system, in terms of the microscopic parameters of our active particles.

C. Prediction of the phase diagram

In this section, we employ the hydrodynamic description obtained in SI Section B to predict the phase diagram of our system (Fig. 4b). We obtain the phase diagram in terms of the microscopic parameters characterizing the self-propulsion and electrostatic interactions of our active particles, which we measure in experiments.

1. Stability of the uniform state. Spinodal lines

The simplest steady state of our active particle suspension is an active gas with a homogeneous particle density $\rho = \rho_0$ and

no polarity, $\mathbf{p} = \mathbf{0}$. In this section, we analyze the stability of this uniform and isotropic state. Thereby, we obtain the spinodal region of the phase diagram, where the uniform state is linearly unstable to phase separation.

To analyze the stability of the uniform state to slow, long-wavelength perturbations, we focus on the density field, which is the only slow variable of the problem. Respectively, the polarity field \mathbf{p} relaxes over a finite time scale D_r^{-1} , becoming adiabatically enslaved to the density field. From Eq. (S44b), and to lowest order in gradients, the polarity tends to

$$\mathbf{p}_{\text{ad}} = \frac{1}{2D_r} (v_{\text{tor}}[\rho] \nabla \rho - \nabla (v[\rho] \rho)). \quad (\text{S46})$$

Introducing this expression into Eq. (S44a), we obtain a closed equation for the density field, which can be written as

$$\partial_t \rho = -\nabla \cdot \mathbf{J}; \quad \mathbf{J} = -\mathcal{D}[\rho] \nabla \rho, \quad (\text{S47})$$

where

$$\mathcal{D}[\rho] = D_t + D_{\text{rep}}[\rho] + \frac{v[\rho]}{2D_r} (v[\rho] + v'[\rho] \rho - v_{\text{tor}}[\rho]) \quad (\text{S48})$$

is a collective diffusivity functional.

Based on Eq. (S47), density perturbations $\delta \rho(\mathbf{r}, t) = \rho(\mathbf{r}, t) - \rho_0$ around the uniform density ρ_0 evolve as

$$\partial_t \delta \rho = \mathcal{D}(\rho_0) \nabla^2 \delta \rho. \quad (\text{S49})$$

Thus, the uniform state experiences a spinodal instability for $\mathcal{D}(\rho_0) < 0$. In the absence of interaction torques ($v_{\text{tor}}[\rho] = 0$), the collective diffusivity $\mathcal{D}(\rho_0)$ can turn negative due to the repulsion-induced slowdown, which implies $v'[\rho] < 0$. This effect is the original mechanism for motility-induced phase separation in systems of repulsive self-propelled particles¹. Here, via Eq. (S48), we show that, even in the absence of repulsion-induced slowdown ($v'[\rho] = 0$), interaction torques (with $v'_{\text{tor}} > 0$) can induce motility-induced phase separation.

Including both repulsion and torques, the spinodal lines are determined by the condition $\mathcal{D}(\rho_0) = 0$. In the plane of bare self-propulsion and particle density (v_0, ρ_0), the spinodal lines are given by

$$\begin{aligned} v_0^{\text{sp}} = & \frac{1}{2} \left[(v'_{\text{tor}} - 3v'_{\text{rep}}) \rho_0 \right. \\ & \left. \pm \sqrt{(v'_{\text{tor}} - v'_{\text{rep}})^2 \rho_0^2 - 8D_r(D_t + D'_{\text{rep}} \rho_0)} \right], \end{aligned} \quad (\text{S50})$$

which are shown in blue in Figs. 4b to 4d. Here, based on Eq. (S45), we have defined the density-independent parameters

$$v'_{\text{rep}} = -\zeta_0 / \xi_t < 0, \quad (\text{S51a})$$

$$D'_{\text{rep}} = \zeta_1 / \xi_t > 0, \quad (\text{S51b})$$

$$v'_{\text{tor}} = \tau_1 / \xi_r > 0. \quad (\text{S51c})$$

In Table I, we provide estimates for the values of these parameters in our experiments.

2. Phase coexistence. Binodal lines

The spinodal instability presented in [SI Section C 1](#) leads to phase separation. In this subsection, we build an effective thermodynamic description to predict the densities of the coexisting phases, namely the binodal lines of the phase diagram.

To obtain the binodals, we consider the closed long-time dynamics of the density field given by [Eq. \(S47\)](#). Following previous work^{1,42-45}, we recognize this equation as an effective Cahn-Hilliard equation, which implies the existence of an effective free energy governing phase separation. To obtain this effective free energy, we express the density current in [Eq. \(S47\)](#) as deriving from an effective chemical potential $\mu[\rho]$:

$$\mathbf{J} = -M[\rho]\nabla\mu[\rho] = -M[\rho]\mu'[\rho]\nabla\rho, \quad (\text{S52})$$

where $M[\rho] = \beta D[\rho]\rho$ is the collective mobility associated with the long-time diffusivity $D[\rho]$, with $\beta = 1/(k_B T)$. To obtain this diffusivity, we use that our hydrodynamic description corresponds to a system of self-propelled particles with density-dependent self-propulsion speed $v[\rho]$ and translational diffusion coefficient $D_t + D_{\text{rep}}[\rho]$ (see [Eq. \(S44a\)](#)). These particles undergo a random walk with persistence time D_r^{-1} and with a long-time diffusion coefficient given by

$$D[\rho] = D_t + D'_{\text{rep}}\rho + \frac{v^2[\rho]}{2D_r}. \quad (\text{S53})$$

Using this expression to obtain the mobility $M[\rho]$, and comparing [Eq. \(S52\)](#) with [Eq. \(S47\)](#), we obtain

$$\mu'(\rho) = \frac{\mathcal{D}(\rho)}{M(\rho)} = \frac{k_B T}{\rho} \left[1 + \frac{\frac{v(\rho)}{2D_r} [v'_{\text{rep}} - v'_{\text{tor}}]\rho}{D_t + D'_{\text{rep}}\rho + \frac{v^2(\rho)}{2D_r}} \right]. \quad (\text{S54})$$

Integrating over ρ , we obtain the chemical potential

$$\begin{aligned} \beta\mu(\rho) &= \ln \rho + \frac{1}{2} \left[1 - \frac{v'_{\text{tor}}}{v'_{\text{rep}}} \right] \ln D(\rho) \\ &+ \frac{D_r D'_{\text{rep}} [1 - v'_{\text{tor}}/v'_{\text{rep}}]}{\sqrt{D_r^2 (D'_{\text{rep}})^2 + 2v'_{\text{rep}} D_r (v_0 D'_{\text{rep}} - v'_{\text{rep}} D_t)}} \\ &\times \operatorname{arctanh} \left(\frac{D_r D'_{\text{rep}} + v'_{\text{rep}} v(\rho)}{\sqrt{D_r^2 (D'_{\text{rep}})^2 + 2v'_{\text{rep}} D_r (v_0 D'_{\text{rep}} - v'_{\text{rep}} D_t)}} \right) \end{aligned} \quad (\text{S55})$$

up to an irrelevant constant term. Assuming that the free energy density $f(\rho)$ is a local function of the density, it obeys

$f'(\rho) = \mu(\rho)$. Integrating this equation, we obtain

$$\begin{aligned} \beta f(\rho) &= \rho(\ln \rho - 1) \\ &+ \frac{1}{2} \left[1 - \frac{v'_{\text{tor}}}{v'_{\text{rep}}} \right] \left[\rho + \frac{2D_r D'_{\text{rep}} + v_0 v'_{\text{rep}}}{(v'_{\text{rep}})^2} \right] \ln D(\rho) \\ &+ \frac{D_r D'_{\text{rep}} [1 - v'_{\text{tor}}/v'_{\text{rep}}] \left[\rho + \frac{2D_r D'_{\text{rep}} + 3v_0 v'_{\text{rep}}}{(v'_{\text{rep}})^2} - \frac{2D_t}{D'_{\text{rep}}} \right]}{\sqrt{D_r^2 (D'_{\text{rep}})^2 + 2v'_{\text{rep}} D_r (v_0 D'_{\text{rep}} - v'_{\text{rep}} D_t)}} \\ &\times \operatorname{arctanh} \left(\frac{D_r D'_{\text{rep}} + v'_{\text{rep}} v(\rho)}{\sqrt{D_r^2 (D'_{\text{rep}})^2 + 2v'_{\text{rep}} D_r (v_0 D'_{\text{rep}} - v'_{\text{rep}} D_t)}} \right) \end{aligned} \quad (\text{S56})$$

up to irrelevant terms linear in the density ρ . The thermodynamic pressure can then be obtained as $p(\rho) = \mu(\rho)\rho - f(\rho)$, giving

$$\begin{aligned} \beta p(\rho) &= \rho + \left[1 - \frac{v'_{\text{tor}}}{v'_{\text{rep}}} \right] \left[\rho - \frac{1}{2} \frac{2D_r D'_{\text{rep}} + v_0 v'_{\text{rep}}}{(v'_{\text{rep}})^2} \right] \ln D(\rho) \\ &- \frac{D_r D'_{\text{rep}} [1 - v'_{\text{tor}}/v'_{\text{rep}}] \left[\frac{2D_r D'_{\text{rep}} + 3v_0 v'_{\text{rep}}}{(v'_{\text{rep}})^2} - \frac{2D_t}{D'_{\text{rep}}} \right]}{\sqrt{D_r^2 (D'_{\text{rep}})^2 + 2v'_{\text{rep}} D_r (v_0 D'_{\text{rep}} - v'_{\text{rep}} D_t)}} \\ &\times \operatorname{arctanh} \left(\frac{D_r D'_{\text{rep}} + v'_{\text{rep}} v(\rho)}{\sqrt{D_r^2 (D'_{\text{rep}})^2 + 2v'_{\text{rep}} D_r (v_0 D'_{\text{rep}} - v'_{\text{rep}} D_t)}} \right). \end{aligned} \quad (\text{S57})$$

up to an irrelevant constant. These three effective thermodynamic functions, namely the chemical potential $\mu(\rho)$, the free energy density $f(\rho)$, and the pressure $p(\rho)$ are plotted in [Fig. S11](#).

Leveraging this effective thermodynamic picture, we obtain the binodal lines by building a common-tangent construction on the effective free energy $f(\rho)$ ([Fig. S11a](#)). Given that $f(\rho) = \mu(\rho)\rho - p(\rho)$, the common-tangent construction corresponds to requiring coexisting phases to have equal chemical potential and pressure,

$$\mu(\rho_g) = \mu(\rho_l), \quad p(\rho_g) = p(\rho_l), \quad (\text{S58})$$

where ρ_g and ρ_l are the densities of the coexisting (gas and liquid) phases ([Figs. S11b](#) and [S11c](#)). Alternatively, the common-tangent construction also amounts to performing the Maxwell construction on the curve $p(1/\rho)$ ([Fig. S11d](#)). In practice, we solve [Eq. \(S58\)](#) numerically and obtain the binodal lines shown in red in [Figs. 4b](#) and [4c](#).

Using the thermodynamic framework presented above, we obtain the spinodal lines from the inflection points of the effective free energy, given by condition $f''(\rho) = 0$. The spinodal lines obtained in this way coincide with the results of the linear stability analysis in [SI Section C 1](#), confirming the consistency of our thermodynamic approach.

Finally, although qualitatively correct, the binodals obtained from the common-tangent construction above have

been shown to fail to accurately reproduce the coexisting densities measured in simulations of active Brownian particles^{1,5,46–48,59}. In recent work, Solon et al. have developed a theory to predict quantitatively-accurate binodals for systems of active Brownian particles^{47,48}. In that framework, the non-equilibrium corrections to the common-tangent construction stem from the fact that the effective chemical potential is a non-local functional of the density, including density-gradient terms that describe interfaces^{1,43,47,48}. While it is in principle possible to obtain these terms by means of a gradient expansion of Eqs. (S30) and (S44b) to order higher than we did in SI Section B 2, this calculation falls beyond the scope of our work.

D. Parameter estimates

In this section, we provide experimental estimates for the parameters of the model, which we list in Table I. In the first part of Table I, we collect estimates for parameters that are measured quantities. In the second part of Table I, we collect the formulae to derive other parameter values from the measured parameters as explained below. In the third part of Table I, we collect the formulae and values of interaction parameters obtained numerically using the experimentally measured pair distribution function (Fig. S10) as explained below.

Some of the estimates in the first part of Table I do not come from direct measurements in our experimental system. In particular, we estimate the viscosity η and the relative dielectric permittivity ϵ_r of the solvent to be those of water at room temperature. Respectively, we estimate the electrostatic screening length λ to be given by the distance between the electrodes in

the experimental setup. Finally, the dielectric permittivity of vacuum, ϵ_0 , is a fundamental constant.

The rest of estimates in the first part of Table I are obtained by direct measurements in our experimental system. In particular, rotational fluctuations stem mainly from imperfections of the electrode surface, which slightly redirect particle motion over short time scales. Hence, the rotational diffusion coefficient D_r needs not be related to the rotational friction coefficient ξ_r , which is mainly due to viscous drag from the solvent. From tracks of single-particle orientation at low particle densities, we measure $D_r \approx 0.15 \text{ s}^{-1}$ (Fig. 2c). This value reflects the non-thermal origin of rotational fluctuations; it is larger than the thermal value derived from the rotational Stokes-Einstein relation $D_r^{\text{SE}} = k_B T / \xi_r$, with $\xi_r = 8\pi\eta R^3$ for a spherical particle of radius R , which gives $D_r^{\text{SE}} \approx 0.05 \text{ s}^{-1}$.

In the second part of Table I, we estimate the bare translational diffusion coefficient D_t of our particles via the translational Stokes-Einstein relation $D_t = K_B T / \xi_t$, with $\xi_t = 6\pi\eta R$ the viscous drag coefficient of a sphere of radius R . We obtain a bare diffusion coefficient $D_t \approx 0.16 \mu\text{m}^2$, which is much smaller than the active contribution $v_0^2 / (2D_r)$ to the long-time diffusion coefficient of a self-propelled particle.

Finally, in the third part of Table I, we provide estimates for the coefficients ζ_0 , ζ_1 , and τ_1 , which characterize the different contributions to the collective interaction force and torque. To estimate these coefficients, we numerically evaluated the integrals in Eq. (S37) using the experimentally measured pair correlation function $g(r, \phi)$ (Fig. S10). For convenience, we also provide estimates for other interaction coefficients directly derived from ζ_0 , ζ_1 , and τ_1 (see Eqs. (S45) and (S51)).

Description	Estimate
Particle radius	$R \approx 1.5 \mu\text{m}$
Self-propulsion speed	$v_0 \approx 10 - 40 \mu\text{m/s}$
Area fraction of particles	$\phi_0 \approx 0.15$
Solvent viscosity	$\eta \approx 0.89 \text{ mPa}\cdot\text{s}$
Rotational diffusion coefficient	$D_r \approx 0.15 \text{ s}^{-1}$
Voltage amplitude	$V_0 = 10 \text{ V}$
Electric field frequency	$\nu = 30 \text{ kHz}$
Electrostatic screening length	$\lambda \approx 120 \mu\text{m}$
Dielectric permittivity of vacuum	$\epsilon_0 \approx 8.85 \cdot 10^{-12} \text{ C}^2/(\text{N m}^2)$
Relative dielectric permittivity of the solvent	$\epsilon_r \approx 78.5$
Real part of the head dipole factor	$\text{Re}[K_h] \approx -0.38$
Imaginary part of the head dipole factor	$\text{Im}[K_h] \approx 0.015$
Real part of the tail dipole factor	$\text{Re}[K_t] \approx 0.28$
Imaginary part of the tail dipole factor	$\text{Im}[K_t] \approx 0.75$
Dipole shift distance	$\ell = 3R/8 \approx 0.56 \mu\text{m}$
Particle number density	$\rho_0 = \phi_0/(\pi R^2) \approx 0.02 \mu\text{m}^{-2}$
Translational drag coefficient	$\xi_t = 6\pi\eta R \approx 25 \text{ mPa}\cdot\text{s}\cdot\mu\text{m}$
Rotational drag coefficient	$\xi_r = 8\pi\eta R^3 \approx 75 \text{ mPa}\cdot\text{s}\cdot\mu\text{m}^3$
Translational diffusion coefficient	$D_t = k_B T/\xi_t \approx 0.16 \mu\text{m}^2/\text{s}$
Electric field amplitude	$E_0 = V_0/\lambda \approx 83 \text{ V/mm}$
Dielectric permittivity of the solvent	$\epsilon = \epsilon_r \epsilon_0 \approx 6.95 \cdot 10^{-10} \text{ C}^2/(\text{N m}^2)$
Repulsion-induced slowdown force coefficient	$\zeta_0 \approx 12 \text{ N}\cdot\mu\text{m}^2, \text{ Eq. (S37a)}$
Repulsion-induced diffusion force coefficient	$\zeta_1 \approx 706 \text{ N}\cdot\mu\text{m}^3, \text{ Eq. (S37b)}$
Interaction torque coefficient	$\tau_1 \approx 300 \text{ N}\cdot\mu\text{m}^4, \text{ Eq. (S37c)}$
Repulsion-induced slowdown effective speed	$v_{\text{rep}} = \zeta_0 \rho_0 / \xi_t \approx 10 \mu\text{m/s}$
Repulsion-induced effective diffusivity	$D_{\text{rep}} = \zeta_1 \rho_0 / \xi_t \approx 595 \mu\text{m}^2/\text{s}$
Torque-induced effective speed	$v_{\text{tor}} = \tau_1 \rho_0 / \xi_r \approx 84 \mu\text{m/s}$
Repulsion-induced slowdown slope	$v'_{\text{rep}} = -\zeta_0 / \xi_t / (\pi R^2) \approx -68 \mu\text{m/s}$
Repulsion-induced diffusivity slope	$D'_{\text{rep}} = \zeta_1 / \xi_t / (\pi R^2) \approx 3970 \mu\text{m}^2/\text{s}$
Torque-induced speed slope	$v'_{\text{tor}} = \tau_1 / \xi_r / (\pi R^2) \approx 561 \mu\text{m/s}$

Table 1 | Experimental estimates of parameters. The first part of the table lists estimates for parameters that are measured quantities. See [SI Section A 1](#) for the definition of the dipole factors. The second part of the table lists the formulae and estimates for parameters that are not directly measured but derived from other parameters. The third part of the table lists the formulae and values of parameters obtained from the measured pair distribution function ([Fig. S10](#), see text). The last six quantities follow from the first three. The slope quantities at the end of the table, indicated with a prime, are defined here with respect to the area fraction ϕ , not the particle concentration ρ .